


Large suppression of spin-relaxation rate in graphene nanoribbons in the presence of magnetic impurities

Van Minh Nguyen^{*} and C. S. Chu[†]

Department of Electrophysics, National Yang Ming Chiao Tung University, Hsinchu 30010, Taiwan

 (Received 23 February 2022; revised 15 April 2022; accepted 18 April 2022; published 28 April 2022)

Achievement of low spin-relaxation rate is an important goal for spintronics development. We study the spin-relaxation rate arising from a low concentration of magnetic impurities in armchair graphene nanoribbons (AGNR). Large suppression in the spin-relaxation rate, exhibited as dip structures, is found when the Fermi energy approaches a subband band edge. This suppression originated from the quasi-one-dimensional density of states and is manifested via the singular features in the AGNR same-site Green's function $G_{\mathcal{I}\mathcal{I}}$, where \mathcal{I} denotes site locations of magnetic impurities. Analytic analysis of the spin-relaxation rate in the close vicinity of a subband band edge is performed to further reveal the physical nature of the suppression. The robustness of the suppression feature in the spin-relaxation rate is demonstrated by systematically increasing the number of magnetic impurities involved in a coherent multiple scattering with the electrons. Major peaks in the spin-relaxation rate are analyzed in light of their connection with spin-flipped resonances. Competition between magnetic impurities with similar resonance energies is found to lead to suppression in the spin-relaxation rate. Our calculations have taken into account the hydrogen-passivation effects at the AGNR edges when the hopping constant between edge carbons is modified.

DOI: [10.1103/PhysRevB.105.155422](https://doi.org/10.1103/PhysRevB.105.155422)

I. INTRODUCTION

Spin relaxation in graphene has been an subject of intense interest [1]. This is intended for the use of graphene for spintronics [2–4], where the electronic spin degree of freedom is to be utilized for information carriers [5,6]. Empowered by graphene's very low intrinsic spin-orbit coupling, of order μeV [4,7], due to the low atomic number of carbon, and together with its novel transport properties [8,9], graphene has spawned into a graphene and graphene related novel platform material for spintronics [2–4,10–13].

Spin-relaxation time, or spin-relaxation rate (SRR), of graphene systems and structures had been probed experimentally [1,14–26]. Depending on the sample preparation and system configurations, the spin-relaxation time can vary from a subnanosecond [1,15,18,19,22,25] to a few nanoseconds (nsec) [14,17,20,23,24], and even up to tens of nsec [16,21,26]. On the other hand, the spin-relaxation time is expected to be of the order of μsec [10,27], if only effects from the intrinsic spin-orbit coupling of graphene is considered. This large discrepancy in the spin-relaxation time between the experimental findings and the expected intrinsic results had prompted many theoretical studies on nonintrinsic spin relaxation mechanisms in graphene [28–38]. These include spin-relaxation mechanisms associated with adsorbate induced spin-orbit coupling [28–30,33–35], magnetic moments from impurities [29,31,38], spin-orbit coupling from proximity effects [27,36,37], and effects of charged puddles

due to charge impurities residing in the substrate [27,29,38]. Furthermore, contact-induced spin relaxation was observed [39–41]. However, the demonstration that reducing pinholes in the tunnel barriers, the interfacing layer between the spin injectors/detectors and the graphene sheet, leads to the lowering of the spin-relaxation rate [39] has encouraged further studies. More recent effort along this line has fabricated polymer free spin valves by an encapsulation involving hBN on graphene [21], which finding is a fivefold enhancement of the spin-relaxation time. The nonmonotonic dependence of the spin-relaxation time on the carrier density [21] is another finding that suggests a resonant characteristics, such as from magnetic impurities [29,42]. Together with the added features, namely, independence of the spin-relaxation time on the contact resistance area, and the presence of pinholes in the MgO tunnel barriers [21], a physical picture emerges that an appropriate encapsulation reduces the polymer residues and these residues are of the magnetic-scatterer type [4].

That magnetic impurities are much more effective than spin-orbit coupling in becoming the primary source of spin relaxation lends support from both experimental [18,22,23,25] and theoretical [29,31,38,42] results. Isotropy of the SRR for graphene on silicon oxide provides evidences for the dominance of magnetic-impurities over the spin-orbit coupling on the SRR [22,23]. Also the dependence of the SRR on the density of fluorine on graphene also provide another evidence for the role of magnetic scatterers on spin relaxations [25]. Therefore, to meet the target of reaching as low a SRR as is possible, elimination of the magnetic impurities is a key. Yet it is equally important to find ways to lower the SRR for a given sample, whether or not it has already reached a decent low level of magnetic-impurity concentration. Thus

^{*}nguyenminhnhue1991@gmail.com

[†]cschu@nycu.edu.tw

we opt, in this work, to study the tuning for a lower SRR of graphene nanoribbons in the presence of a low concentration of magnetic impurities.

By turning to graphene nanoribbons, we invoke extra multiple scattering effects provided by the quasi-one-dimensional (Q1D) nature of the system for the tuning of the SRR. Conductance of Q1D quantum channels in the presence of attractive scatterers is known, both from theoretical [43] and experimental [44] studies, to exhibit dip structures, and at energies close to but just below subband band edges. The singular density of states at subband band edges provides the impetus for multiple scatterings [43], such that quasibound states are formed when the scatterers are attractive [45]. Recently, Q1D subband band edge effects have been shown [46] to lead to a new description for the Ruderman-Kittel-Kasuya-Yosida (RKKY) type coupling [47–49] between two magnetic impurities in AGNRs. Multiple scattering in the vicinity of a subband band edge plays a key contributing role to RKKY [46]. And large enhancement in the magnitude of the RKKY coupling constant [46], among other changes in its characteristics, is resulted when comparing with that of the lowest-order (Born-type approximation) RKKY coupling constant [50]. Band edge effects on RKKY interaction was found in higher dimension systems such as graphene Bernal bilayers [51]. The energy dependence of the RKKY interaction exhibits remarkable characteristics due to the logarithmic-singular feature in the real-space propagator at a band edge [51].

Multiple scattering arising from the Q1D nature of the AGNR system is expected to occur most characteristically near subband band edges, at energies determined by the AGNR widths. Resonance at the magnetic impurities [29] is another multiple scattering phenomenon, which occurs at energies that depend on the scatterer. The sensitivity of the SRR on the carrier density, or the Fermi energy, would then be high if the SRR is peaked at the resonance [29] and dipped at a subband band edge. It is hence important in this work to see if the SRR is peaked or dipped at subband band edges and to reveal the physics therein.

The magnetic impurity we will consider in this work is the hydrogen adsorbate [29]. It is the simplest adsorbate that is magnetic when adsorbed on graphene [17,29,31,52], and there is a well established tight-binding model describing the hydrogen adsorbate [29,53]. The simplicity in the model also allows us to undergo a comprehensive and detail analytic analysis to reveal the spin-flipping physics for generic magnetic moments in AGNR systems.

We would like to point out that the physical mechanism behind our tuning of the Fermi energy for a lower SRR in AGNRs is conceptually different from the Elliott type “spin hot spot” mechanism in semiconductors [54,55]. The key difference is that our target is a lower SRR whereas that of the spin hot spot is a SRR peak. Another key difference is that the spin-orbit coupling from the crystal lattice is negligible in our case while sufficiently significant bulk spin-orbit coupling is readied in semiconductors. From the work of Elliott [56], the interplay of a spin-diagonal electrostatic interaction, such as from a normal impurity, and the spin mixing in the wave function, due to the crystal lattice spin-orbit coupling, gives rise to spin relaxation in semiconductors [57]. Spin hot

spot occurs on the Fermi surface at the \mathbf{k} point where the crystal lattice spin-orbit coupling becomes comparable with interband energies [58]. In contrast, the physical mechanisms in this work take on multiple scatterings arising both from the Q1D nature of the AGNR system and from magnetic-impurity resonances.

Spin relaxation in AGNRs had been studied recently, where physical quantities of interest were spin-flipped and non-spin-flipped transmissions [59–61] and spin polarizations in the transmission region [60,61]. Both magnetic moment and spin-orbit coupling effects arising from hydrogen adsorbates were considered in a density-functional theory (DFT) based *ab initio* transport formalism [59]. Spin-orbit coupling arising from a Gaussian-type surface in the AGNR due to substrate surface roughness was considered [60]. The ensemble averaged spin-polarization in the transmission region and its dependence on the length of the AGNR were obtained. By fitting this result to an exponential form, decaying with respect to the length of the AGNR, a spin diffusion length was obtained [60]. In a similar way, the spin relaxation length in AGNR doped with nickel adatoms was studied by an *ab initio* approach [61]. The focus was upon the spin-orbit coupling induced by the adatoms. A segmented-AGNR approach for transport was invoked, where each segment contains either one or no adsorbate, such that the entire AGNR, of a given total length and adsorbate concentration, is constructed from randomly arranging these AGNR segments [61]. The adsorbates had been kept from each other by a minimum separation, which was chosen to be 25 Angstrom [61], in order to have negligible adsorbate effects on the coupling between segments.

There is, however, no known relation connecting the spin diffusion (relaxation) length to the spin-relaxation time in AGNRs [61]. Complications due to the subband nature and the difference in the regime of interest, ballistic regime in our case in contrast to strongly disordered regime, have rendered even a heuristic attempt for such a relation not deemed to be feasible. A direct microscopic approach to the SRR in AGNRs is thus lacking and much needed. Such a direct microscopic approach should provide important insights on the key physical mechanisms for the SRR. We formulate in this work a microscopic approach to the SRR in AGNRs and apply it to the case of dilute magnetic impurities.

Highlights of our key SRR results for AGNRs are presented in Fig. 1. The AGNR, of width $W = 20$ (number of longitudinal carbon chains in the AGNR), has its first and second subband band edges at, respectively, $|\mu| = 0.017$ and 0.23 . Energy is in units of t_0 . Between these two subband band edges is a region where there is only one propagating subband. The energy gap at $|\mu| = 0.017$ is resulted from edge passivation [62], without which the energy gap would have been zero. The edge-passivation effects, within the tight-binding description [63,64], have been incorporated to evaluate the AGNR Green’s function and the finite temperature SRR $1/\tau_s$. Our key result, namely, the large SRR suppression, is shown near the second subband band edge (indicated by two downward-pointing arrows), in the $|\mu| \lesssim 0.23$ region, where the SRR exhibits a steep drop to form a dip structure.

The SRR suppression is quantified by a suppression factor F_{sp} , defined as the ratio between the 2D SRR (grey dashed curve) and the finite temperature SRR. In Fig. 1, the

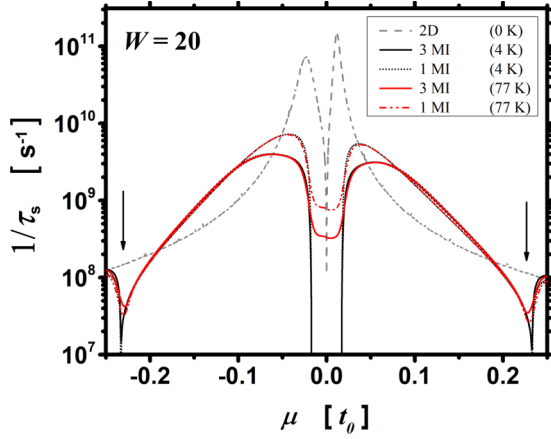


FIG. 1. Spin-relaxation rate (SRR) suppression shown in the AGNR SRR vs chemical potential μ plot. Nanoribbon width $W = 20$. Temperatures shown are 4 (black) and 77 K (red). Incoherent magnetic impurity (MI) cluster (3 MI per cluster, solid curves) and independent MI (dotted and dashed-dotted curves) results for the SRR, given by Eq. (A17), are shown. Energy range $0.017 \leq |\mu| \leq 0.23$ is the one-propagating-subband region. Two-dimensional graphene result (grey dashed curve) is shown for comparison. Large SRR suppression is demonstrated by the rapid drop of the SRR near $|\mu| \approx 0.23$. The two downward pointing arrows indicate where largest SRR suppression occurs. Major SRR peaks around $\mu \approx \pm 0.04$ exhibit another suppression in the SRR. Magnetic impurity fraction $\eta_M = 10^{-6}$.

temperatures are 4 K (black solid curve) and 77 K (red solid curve), and the energies for the F_{sp} are close to the subband band edge ($|\mu| = 0.23$). From Fig. 1, the 4-K suppression factor $F_{sp} = 9.7$ and 9.3 at, respectively, $\mu = \mp 0.23$. And the 77-K suppression factor $F_{sp} = 3.7$ and 3.2 at, respectively, $\mu = \mp 0.23$. The concentration of the magnetic impurities is the same in all curves, given by $\eta_M = 10^{-6}$, the fraction of the AGNR carbon atoms that are adsorbed to by the magnetic impurities. The values of the SRR suppression factor F_{sp} , presented above, is large at 4 K and is quite good even at 77 K.

Robustness of the SRR suppression is demonstrated in Fig. 1. It is by plotting alongside the independent magnetic impurity (MI) results (dashed, dotted, and dashed-dotted curves) for comparison with our incoherent magnetic-impurity cluster results (solid curves). The incoherent MI-cluster results have all intra-cluster electron-MI multiple scatterings fully treated, whereas intercluster electron-MI events are treated incoherently. Results for three magnetic impurities in a cluster are plotted in Fig. 1. As shown in Fig. 1, the independent MI and the incoherent MI-cluster results for the same temperature overlap in most of the μ region, including the SRR suppression region. This lends strong support to the robustness of the SRR suppression feature. Another suppression of the SRR occurs near the two major SRR peaks, near $\mu \approx \pm 0.04$. This is found to associate with the competition between the magnetic impurities for resonances when they have close enough resonance energies. Overall, curves from temperatures 4 and 77 K fall on top of each other except inside the first gap $|\mu| \leq 0.017$ and near the second subband band edge $|\mu| \approx 0.23$. Appropriate ensemble

average has been performed to obtain all our results, and this will be discussed in later sections.

The 2D SRR result shown in Fig. 1 is obtained by taking a large enough W ($W = 6 \times 10^5$ in Fig. 1) for the evaluation of Eq. (23), and it matches that reported in Ref. [29]. Equation (23) is for the independent MI case at zero temperature. The 2D SRR values at 77 K in the $|\mu| \approx 0.23$ region is very close to and slightly greater than the 2D SRR at zero temperature. For simplicity, it suffices to use the zero-temperature 2D SRR to obtain the F_{sp} , when temperatures considered are not much higher than 77 K.

This paper is organized as follows. In Sec. II, we present our theoretical framework for independent MIs in AGNRs. The basic physics associated with the SRR suppression at a subband band edge will be presented. We present our microscopic approach to the SRR in AGNRs. From this approach, we obtain an analytic expression for the SRR suppression near a subband band edge. In addition, we present our analysis showing the resonance nature of the SRR peaks in the large and the small W regimes. In Sec. III, we present our theoretical framework for many MIs. In particular, we present our analytic treatment for two magnetic-impurity case, from which the SRR suppression at a subband band edge remains intact is evident. Extension of the analysis for the SRR suppression at magnetic impurity resonances is presented. We present our systematic study of increasing the number of MIs involved in the multiple scattering. The trend it reveals on the robustness of the SRR suppression at a subband band edge, and on our incoherent MI-cluster approach for the SRR will be presented and discussed. Finally, we present our conclusion in Sec. IV.

II. COHERENT EFFECTS FROM ONE MAGNETIC IMPURITY

This section presents the theoretical treatment for the SRR that arises from independent MIs. In particular, the section presents our microscopic SRR calculation. Both the SRR suppression at a subband band edge, and the resonant nature of the SRR peaks will be presented. Multiple scattering effects between MI will be treated in the next section.

The magnetic impurity is modeled as an adsorbate hydrogen atom, which \hat{H}_{ad} is given by [29]

$$\hat{H}_{ad} = \sum_v [\varepsilon_h h_v^\dagger h_v + T (h_v^\dagger c_{Hv} + c_{Hv}^\dagger h_v)] + J \sum_{v,v'} \sum_i \sigma_{vv'}^i \Sigma^i c_{Hv}^\dagger c_{Hv'}, \quad (1)$$

where h^\dagger (h) and c_H^\dagger (c_H) are the fermionic creation (annihilation) operators for, respectively, orbitals at the site of the hydrogen adsorbate and at the carbon atom to which the hydrogen is adsorbed. The hopping constant between the two orbitals is T , and the energy of the hydrogen orbital is ε_h . The third term is the exchange interaction at the hydrogen-adsorbate site, with σ and Σ , both in the form of Pauli matrix vectors, representing the electron spin and the spin one-half local moment at the hydrogen adsorbate site, respectively. The physics of local moment spin flipping during the electron multiple scattering is thus included. We take the values

$\varepsilon_h = 0.16$ eV, $T = 7.5$ eV, and $J = 0.4$ eV [29]. In the following, all energies are taken to be in units of $t_0 = 2.66$ eV, the hopping constant of graphene.

From using the basis $|j, m\rangle$ of J^2 and J_z , where $\mathbf{J} = \frac{\hbar}{2}(\boldsymbol{\sigma} + \boldsymbol{\Sigma})$, and eliminating the hydrogen-adsorbate orbital, we get

$$\hat{H}_{\text{ad}} = |\mathcal{I}\rangle\langle\mathcal{I}| \otimes \left[\alpha_0 |0, 0\rangle\langle 0, 0| + \alpha_1 \sum_{m=-1}^1 |1, m\rangle\langle 1, m| \right], \quad (2)$$

in which $\alpha_0 = \frac{T^2}{(E - \varepsilon_h + 3J)}$ and $\alpha_1 = \frac{T^2}{(E - \varepsilon_h - J)}$ [29]. We have kept the dependencies of α_0 and α_1 on the electron energy E implicit for the simplicity in the presentation. By the same token, whenever a physical quantity is well understood to depend on energy, we might choose to keep its energy dependence implicit. The singular energy dependencies in α_0 and α_1 correctly reflect the hydrogen-adsorbate site energy levels, namely, $\varepsilon_h - 3J$ (singlet level) and $\varepsilon_h + J$ (triplet level), respectively, when the exchange interaction is included. In addition, $|\mathcal{I}\rangle = |i, s\rangle$ depicts the site lattice of the carbon atom to which the hydrogen is adsorbed, where $(i, s) = (\mathbf{R}_i, s)$ are, respectively, the unit-cell position and the site-type (A/B type) index.

Converting Eq. (2) to the spin configuration basis ket $|v, u\rangle$, where $v = \pm$ and $u = \pm$ are the eigenvalues of σ_z and Σ_z , respectively, we have

$$\hat{H}_{\text{ad}} = |\mathcal{I}\rangle\langle\mathcal{I}| \otimes \left[\sum_{v,u} V_{vu}^{\text{nf}} |v, u\rangle\langle v, u| + \sum_v V_0^f |\bar{v}, v\rangle\langle v, \bar{v}| \right], \quad (3)$$

in which $V_{vu}^{\text{nf}} = \frac{T^2[E - \varepsilon_h + (vu + 2)J]}{(E - \varepsilon_h + 3J)(E - \varepsilon_h - J)}$ indicates two types of non-spin-flipping potential. The $u = \bar{v}$ case has non-spin-flipping potential $V_0^{\text{nf}} = (\alpha_0 + \alpha_1)/2$, while the $u = v$ case has non-spin-flipping potential $V_1^{\text{nf}} = \alpha_1$. Here $\bar{v} = -v$. On the other hand, the spin-flipping potential is $V_0^f = (\alpha_1 - \alpha_0)/2$. The form of \hat{H}_{ad} in Eq. (3) is appropriate for treating cases of multiple scattering between MIs, as will be used in the next section.

Spin-flipped multiple scattering of an electron by a single magnetic impurity in an AGNR is treated below. Equation (3) shows that spin-flipping occurs only for incident spin configuration $|v, \bar{v}\rangle$, thus we consider an incident state (right-going) $|\psi_{\mathbf{k}_n}\rangle \otimes |v, \bar{v}\rangle$, where the orbital part $|\psi_{\mathbf{k}_n}\rangle$ is given by Eq. (B5). The resulting scattering state $|\Psi_{\mathbf{k}_n, v\bar{v}}\rangle$ is of the form

$$|\Psi_{\mathbf{k}_n, v\bar{v}}\rangle = |\Psi_{\mathbf{k}_n, v\bar{v}}^{\text{nf}}\rangle \otimes |v, \bar{v}\rangle + |\Psi_{\mathbf{k}_n, v\bar{v}}^{\text{f}}\rangle \otimes |\bar{v}, v\rangle, \quad (4)$$

where the first (second) term corresponds to the non-spin-flipped (flipped) component of the scattering state. The Lippmann-Schwinger equation is given by

$$|\Psi_{\mathbf{k}_n, v\bar{v}}\rangle = |\psi_{\mathbf{k}_n}\rangle \otimes |v, \bar{v}\rangle + \hat{G}\hat{H}_{\text{ad}}|\Psi_{\mathbf{k}_n, v\bar{v}}\rangle, \quad (5)$$

where \hat{G} is the AGNR Green's function presented in Eq. (B6). Projecting Eq. (5) onto $|\mathcal{I}\rangle \otimes \langle v', \bar{v}'|$ leads to

$$\begin{aligned} \Psi_{\mathbf{k}_n, v\bar{v}}^{\text{nf}}(\mathcal{I}) &= \psi_{\mathbf{k}_n}(\mathcal{I}) + G_{\mathcal{I}\mathcal{I}}(E) V_0^{\text{nf}} \Psi_{\mathbf{k}_n, v\bar{v}}^{\text{nf}}(\mathcal{I}) \\ &\quad + G_{\mathcal{I}\mathcal{I}}(E) V_0^f \Psi_{\mathbf{k}_n, v\bar{v}}^{\text{f}}(\mathcal{I}) \end{aligned} \quad (6)$$

and

$$\Psi_{\mathbf{k}_n, v\bar{v}}^{\text{f}}(\mathcal{I}) = G_{\mathcal{I}\mathcal{I}}(E) V_0^{\text{nf}} \Psi_{\mathbf{k}_n, v\bar{v}}^{\text{nf}}(\mathcal{I}) + G_{\mathcal{I}\mathcal{I}}(E) V_0^f \Psi_{\mathbf{k}_n, v\bar{v}}^{\text{f}}(\mathcal{I}). \quad (7)$$

The form of Eq. (6) is physically self-explanatory. It shows that the non-spin-flipped component at the site $|\mathcal{I}\rangle$ of the hydrogen-adsorbed carbon atom is constituted of three terms: the incident wave at $|\mathcal{I}\rangle$, the same-site propagation after the non-spin-flipped component suffers a non-spin-flipped scattering at $|\mathcal{I}\rangle$, and the same-site propagation after the spin-flipped component suffers a spin-flipped scattering at $|\mathcal{I}\rangle$. One can apply this physical interpretation to Eq. (7), except that there are now only two terms.

Solving Eqs. (6) and (7) gives us

$$\Psi_{\mathbf{k}_n, v\bar{v}}^{\text{nf}}(\mathcal{I}) = \frac{1}{2} \left[\frac{1}{1 - \alpha_1 G_{\mathcal{I}\mathcal{I}}} + \frac{1}{1 - \alpha_0 G_{\mathcal{I}\mathcal{I}}} \right] \psi_{\mathbf{k}_n}(\mathcal{I}) \quad (8)$$

and

$$\Psi_{\mathbf{k}_n, v\bar{v}}^{\text{f}}(\mathcal{I}) = \frac{(\alpha_1 - \alpha_0) G_{\mathcal{I}\mathcal{I}}}{2(1 - \alpha_1 G_{\mathcal{I}\mathcal{I}})(1 - \alpha_0 G_{\mathcal{I}\mathcal{I}})} \psi_{\mathbf{k}_n}(\mathcal{I}). \quad (9)$$

Equation (9) can also be cast in a form similar to Eq. (8), where the sign of the second term in Eq. (8) is reversed.

Subband band-edge features enter Eqs. (8) and (9) via the same-site Green's function $G_{\mathcal{I}\mathcal{I}}$, which carries in it the quasi-one-dimensional nature of the AGNRs, where density of states are singular at subband band edges. Additional subband band-edge feature might enter later in the SRR calculation, but Eqs. (8) and (9) are sufficient to provide us physical insights about our key results in this work. The key physics we find in this work is the large suppression of the spin-relaxation rate when the electron energy $|E|$ approaches a subband band edge.

Two important features can be obtained from Eqs. (8) and (9). The first feature is about the suppression of both $\Psi_{\mathbf{k}_n, v\bar{v}}^{\text{nf}}(\mathcal{I})$ and $\Psi_{\mathbf{k}_n, v\bar{v}}^{\text{f}}(\mathcal{I})$ when E approaches a subband bottom. As $|E|$ approaches the n th subband band edge $\varepsilon_{n, \text{min}}$ while staying within the subband energy range, the corresponding reduced Green's function $g_n^{\mathcal{I}\mathcal{I}}(E)$ increases in its magnitude and dominates the behavior of the $G_{\mathcal{I}\mathcal{I}}$. This is due to the vanishing of the longitudinal wave vector Q_n , as is shown in Eq. (B7), given by

$$g_n^{\mathcal{I}\mathcal{I}}(E) = -i \frac{\pi |E|}{2\beta_n (1 + \Delta h_n) \sin Q_n}. \quad (10)$$

Here $\beta_n = -\cos(k_{nx}a)$, and $k_{nx} = n\pi / [(W + 1)a]$ is the quantized transverse wave vector (see Appendix B). Of particular interest is the $n = n_0 = 2(W + 1)/3$ subband for the $W = 3p + 2$ AGNRs, which would be gapless if edge passivation were not included. On the other hand, for the case when $|E|$ approaches the subband band edge with $|E| \lesssim \varepsilon_{n, \text{min}}$, it is outside the n th subband energy range, we have $Q_n = i\gamma Q_{n1}$, the evanescent wave vector. As Q_{n1} approaches zero, the reduced Green's function $g_n^{\mathcal{I}\mathcal{I}}$ also increases in its magnitude and dominates $G_{\mathcal{I}\mathcal{I}}$. Here $\gamma = E/|E|$. Explicitly, from Eqs. (8) and (9), and for E in the close vicinity of a subband band edge, we have $\Psi_{\mathbf{k}_n, v\bar{v}}^{\text{nf}}(\mathcal{I}) \approx -\frac{\alpha_0 + \alpha_1}{2\alpha_0\alpha_1} G_{\mathcal{I}\mathcal{I}}^{-1} \psi_{\mathbf{k}_n}(\mathcal{I})$, and $\Psi_{\mathbf{k}_n, v\bar{v}}^{\text{f}}(\mathcal{I}) \approx \frac{\alpha_1 - \alpha_0}{2\alpha_0\alpha_1} G_{\mathcal{I}\mathcal{I}}^{-1} \psi_{\mathbf{k}_n}(\mathcal{I})$. The suppression factor is $G_{\mathcal{I}\mathcal{I}}^{-1}$. We emphasize that this suppression is the result of multiple scatterings. More accurately, it is the above-mentioned subband band edge singular feature of $G_{\mathcal{I}\mathcal{I}}$ that has demanded the need of the multiple scattering, and resulting in the suppression.

The scattered waves are obtained from projecting Eq. (5) onto $\langle \mathcal{J} | \otimes \langle \nu\bar{\nu} |$, at an arbitrary lattice site $|\mathcal{J}\rangle$, and together with Eqs. (8) and (9), we get

$$\Psi_{\mathbf{k}_n, \nu\bar{\nu}}^{\nu\bar{\nu}}(\mathcal{J}) = \psi_{\mathbf{k}_n}(\mathcal{J}) + G_{\mathcal{J}\mathcal{I}} \frac{\alpha_1 + \alpha_0 - 2\alpha_0\alpha_1 G_{\mathcal{I}\mathcal{I}}}{2\mathcal{D}(E, \mathcal{I})} \psi_{\mathbf{k}_n}(\mathcal{I}) \quad (11)$$

and

$$\Psi_{\mathbf{k}_n, \nu\bar{\nu}}^{\bar{\nu}\nu}(\mathcal{J}) = G_{\mathcal{J}\mathcal{I}} \frac{\alpha_1 - \alpha_0}{2\mathcal{D}(E, \mathcal{I})} \psi_{\mathbf{k}_n}(\mathcal{I}), \quad (12)$$

where $\mathcal{D}(E, \mathcal{I}) = (1 - \alpha_1 G_{\mathcal{I}\mathcal{I}})(1 - \alpha_0 G_{\mathcal{I}\mathcal{I}})$.

We note that very different subband band-edge *suppression* characteristics are exhibited in the two scattered-wave components, in Eqs. (11) and (12). The non-spin-flipped component consists of a $G_{\mathcal{I}\mathcal{I}}^{-1}$ suppression, arising from the coefficient to the $G_{\mathcal{J}\mathcal{I}}$ term in Eq. (11). On the other hand, the spin-flipped component consists of a $G_{\mathcal{I}\mathcal{I}}^{-2}$ suppression in Eq. (12). The propagating channels contained in $G_{\mathcal{J}\mathcal{I}}$, when $|E| \lesssim \varepsilon_{n, \min}$ and \mathcal{J} is outside the scattering region, do not contribute additional of the aforementioned near band edge singular feature. Therefore the source amplitudes of the outgoing scattered waves carry a $G_{\mathcal{I}\mathcal{I}}^{-2}$ ($G_{\mathcal{I}\mathcal{I}}^{-1}$) suppression factor for the spin-flipped (non-spin-flipped) component. This is due to the presence (absence) of the interference between the $j = 0$ and $j = 1$ processes, as is evident by the $\alpha_0\alpha_1$ factor in Eq. (11), in the non-spin-flipped (spin flipped) component. Hence the interplay between the interference processes and the subband feature of the system has brought forth a stronger suppression to the outgoing spin-flipped scattered wave than the outgoing non-spin-flipped scattered wave for the single MI case.

The second feature obtained from Eqs. (8) and (9) is about the resonance of the MI. Assuming that the resonance conditions are given by $\text{Re}(1 - \alpha_j G_{\mathcal{I}\mathcal{I}}) = 0$, according to Eqs. (8) and (9), the resonance energies E_R could then be determined approximately as $E_{R, j}^0$. These resonances are associated with the spin-configurations, triplet ($j = 1$) or singlet ($j = 0$).

Approximate expression $E_{R, j}^0$ obtained in the following reveals the dependence of the physical nature of the SRR peaks on W . Assuming the magnitude of $E_{R, j}^0$ to be much less than the second subband band edge, then from the reduced Green's functions in Eq. (B9) and Eq. (B11), we have

$$G_{\mathcal{I}\mathcal{I}}(E) \approx -E \zeta_1 - i\zeta_2, \quad (13)$$

where $\zeta_1 = \sum_{n \neq n_0} \frac{\varphi_n^2(i)}{|4\beta_n^2 - (1 + \Delta h_n)^2|}$, and $\zeta_2 = \frac{\varphi_{n_0}^2(i)}{2\sqrt{1 + \Delta h_{n_0}}}$. The Δh_n , given in Eq. (B4), arises from the edge passivation. The two terms in Eq. (8) are then cast into a resonance form

$$\frac{1}{1 - \alpha_j G_{\mathcal{I}\mathcal{I}}} = \frac{A_j}{E - E_{R, j}^0 + i\Gamma}, \quad (14)$$

where A_j is a simple coefficient not essential to the resonance feature, and

$$E_{R, j}^0 = \frac{\varepsilon_j}{1 + T^2 \zeta_1}. \quad (15)$$

The energy ε_j equals $\varepsilon_h - 3J$ and $\varepsilon_h + J$ for, respectively, $j = 0$ and 1. The resonance width is $\Gamma = \frac{T^2}{1 + T^2 \zeta_1} \zeta_2$. It provides us the condition for the two resonances to be resolved, which is

$E_{R, 1}^0 - E_{R, 0}^0 > \Gamma$, or the condition

$$\frac{4J}{T^2} > \zeta_2. \quad (16)$$

At $E = E_{R, 0}^0$, we can drop the term $\frac{1}{1 - \alpha_1 G_{\mathcal{I}\mathcal{I}}}$ in Eqs. (8) and (9) to obtain $\Psi_{\mathbf{k}_n, \nu\bar{\nu}}^{\nu\bar{\nu}}(\mathcal{I}) = -\Psi_{\mathbf{k}_n, \nu\bar{\nu}}^{\bar{\nu}\nu}(\mathcal{I})$. Similarly, at $E = E_{R, 1}^0$, we obtain $\Psi_{\mathbf{k}_n, \nu\bar{\nu}}^{\nu\bar{\nu}}(\mathcal{I}) = \Psi_{\mathbf{k}_n, \nu\bar{\nu}}^{\bar{\nu}\nu}(\mathcal{I})$. This is consistent with the singlet and triplet nature of the $j = 0$ and $j = 1$ cases, respectively.

The condition for the two resonances to be resolved is satisfied at large W cases, since φ_{n_0} [Eq. (B2)] in ζ_2 decreases with W in the form $1/\sqrt{W + 1}$. For small W , when Eq. (16) is not satisfied, the resonance condition becomes

$$\frac{d|\mathcal{D}(E, \mathcal{I})|}{dE} = 0, \quad (17)$$

from which the SRR peaks at E_R are resonances with a j -mixed nature. We will present numerical examples for j -resolved ($W = 98$) and j -mixed ($W = 20$) resonance SRR peaks.

A. Spin-relaxation rate from transport calculation

In this section, we calculate the spin-relaxation rate within a quantum transport approach. The approach is formally established in Appendix A. It involves an extraction of the spin-flipped transmission and reflection coefficients from Eq. (12). And it also involves the use of the coefficients to obtain the spin-relaxation rate $R_s(n', \mathbb{S}'; n, \mathbb{S})$, as defined in Eq. (A11), for the specific spin-flipping process, from the initial state (n, \mathbb{S}) to final state (n', \mathbb{S}') at energy E . Here \mathbb{S} denotes the system spin configuration, including that of the electron and the magnetic impurity, and n (n') denotes the incident (outgoing) propagating subband index. The spin-relaxation rate for a specific spin-flipped process is used for the calculation of the spin-relaxation rate τ_s^{-1} when thermal and system configuration averaging are to be performed.

Extraction of the spin-flipped transmission coefficients from $\Psi_{\mathbf{k}_n, \nu\bar{\nu}}^{\bar{\nu}\nu}(\mathcal{J})$ is done by substituting the Green's function [Eq. (B6)] into Eq. (12), focusing on the outgoing propagation channels (n') in $G_{\mathcal{J}\mathcal{I}}$, choosing the longitudinal coordinate N_j of the observation point $|\mathcal{J}\rangle$ to be greater than N_i of the magnetic impurity location $|\mathcal{I}\rangle$, and casting each such terms into the form $t_{n'n}^f(\mathbb{S}', \mathbb{S})\psi_{\mathbf{k}_{n'}}(\mathcal{J})$.

Using Eqs. (B5) and (B7), and following the method laid out in Eq. (A8), we get

$$\begin{aligned} t_{n'n}^f(\bar{\mathbb{S}}, \mathbb{S}) &= \frac{\alpha_1 - \alpha_0}{4\pi\mathcal{D}(E, \mathcal{I})} \varphi_{n'}(i)\varphi_n(i) g_{n'}^{\mathcal{I}\mathcal{I}}(E) \\ &\times \frac{C^{S_i}(\mathbf{k}_n)}{C^{S_i}(\mathbf{k}_{n'})} e^{i\gamma(Q_n - Q_{n'})N_i}, \end{aligned} \quad (18)$$

where $\bar{\mathbb{S}}$ is $(\bar{\nu}\nu)$ when \mathbb{S} denotes $(\nu\bar{\nu})$. We have chosen, for convenience, that $|\mathcal{I}\rangle$ and $|\mathcal{J}\rangle$ are of the same site type.

The spin-flipped reflection coefficient can be derived similarly, except that we need to choose $N_j < N_i$ and the outgoing state becomes $\psi_{\mathbf{k}_n^-}(\mathcal{J})$. We obtain

$$|r_{n'n}^f(\bar{\mathbb{S}}, \mathbb{S})|^2 = |t_{n'n}^f(\bar{\mathbb{S}}, \mathbb{S})|^2. \quad (19)$$

Equation (18) does not depend on ν reflects the symmetry of the SRR with respect to the reversing of the initial system spin configuration.

The process-specific SRR, following Eq. (A11), is given by

$$R_s(n', \bar{S}; n, S) = \frac{2 v_{gn'}(E)}{N_y \sqrt{3} a} |t_{n'n}^f(\bar{S}, S)|^2, \quad (20)$$

which, according to Appendix A, is the spin-flipped current for the corresponding transition processes. Here $v_{gn'}(E)$ is the group velocity of the outgoing n' th subband. The corresponding zero-temperature SRR $R_s^0(n', \bar{S}; S)$, as is shown in Eq. (A13), is given by

$$R_s^0(n', \bar{S}; S) = \frac{\sum_n' \frac{1}{v_{gn'}} R_s(n', \bar{S}; n, S)}{\sum_n' \frac{1}{v_{gn'}}}. \quad (21)$$

The SRR $1/\tau_s^0$ at zero temperature and chemical potential μ is then given by

$$\frac{1}{\tau_s^0} = \frac{\mathcal{N}_M}{\mathcal{N}_S} \sum_S \left\langle \sum_{n'}' R_s^0(n', \bar{S}; S) \right\rangle_{\mathcal{I}}, \quad (22)$$

where we have included averagings over both the incident system-spin configuration as well as the magnetic impurity transverse locations $|\mathcal{I}|$. Here $\mathcal{N}_M = \eta_M \mathcal{N}_C$ is the total number of magnetic impurity, $\mathcal{N}_C = W N_y$ is the total number of carbon atoms in the AGNR, and η_M is the fraction of carbon atoms being adsorbed to by the MIs. \mathcal{N}_S is the total number of spin configurations [4 in this case, when $S = (\nu\nu)$ are also included]. For our case here, the spin-relaxation rate will be zero when $S = (\uparrow\uparrow)$ or $S = (\downarrow\downarrow)$.

We note that $N_y/2$ is the total number of AGNR unit cells, $N_y \sqrt{3} a$ is the total length of the AGNR, and a is the separation between adjacent longitudinal carbon chain.

The expression for the zero-temperature SRR $1/\tau_s^0$ is obtained from Eqs. (22), (18), and (20), to give

$$\frac{1}{\tau_s^0} = \frac{\eta_M}{2\hbar} (\alpha_1 - \alpha_0)^2 |\mu| \sum_{M_i=0}^{W-1} \frac{\xi(\mu, \mathcal{I})}{|\mathcal{D}(\mu, \mathcal{I})|^2}, \quad (23)$$

where the summation over M_i arises from the transverse MI-position average, and

$$\xi(\mu, \mathcal{I}) = \frac{\sum_n' \sum_{n'}' \frac{\varphi_n^2(i) \varphi_{n'}^2(i)}{\beta_n(1+\Delta h_n) \sin Q_n \beta_{n'}(1+\Delta h_{n'}) \sin Q_{n'}}}{16 \sum_n' \frac{1}{\beta_n(1+\Delta h_n) \sin Q_n}}. \quad (24)$$

The primed summation denotes summing only over propagating subbands.

B. Numerical examples

We plot in Fig. 2 the zero-temperature SRR of two AGNRs. The plot is intended to display the SRR dip structures near subband band edges and to provide explicit illustrations of the resonance nature of the major SRR peaks. For these purposes, it is sufficient to treat the MIs as independent MIs. Two AGNRs shown have $W = 20$ (red curve) and $W = 98$ (black curve). The SRR dip structures are found to occur at subband band edges, where the $W = 98$ curve has narrower subband

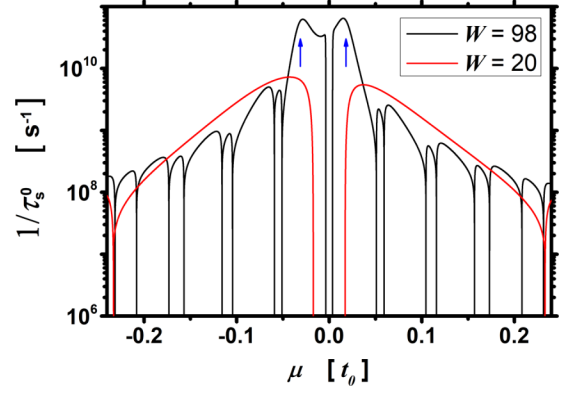


FIG. 2. Zero-temperature SRR $1/\tau_s^0$ due to independent MIs in AGNRs. Equation (23) has been used for the $1/\tau_s^0$. Cases for $W = 20$ (red) and 98 (black) AGNRs are shown. Averaging over impurity transverse positions, incident subbands, and spin configurations have been performed to obtain the SRR. All dip structures in the SRR are aligned with subband band edges. Large SRR suppressions as μ approaches a subband band edge are shown for both curves. Major SRR-peak energies in (1) the $W = 98$ case (depicted by two arrows) match with the $E_{R,j}^0$ in Eq. (15), and (2) the $W = 20$ case match with the resonance energies obtained from the condition in Eq. (17). The magnetic impurity fraction $\eta_M = 10^{-6}$.

band-edge spacings than that for the $W = 20$ curve. All the subband band edges shown in Fig. 2 are the $\varepsilon_{n,\min}$, the lower band edge of the n th subband. In particular, the lowest two band edges (closest to $\mu = 0$) are at $|\mu| = 0.0036$ ($n_0 = 66$) and $|\mu| = 0.054$ ($n_1 = 67$) for $W = 98$. As for $W = 20$, the lowest two band edges are at $|\mu| = 0.017$ ($n_0 = 14$) and $|\mu| = 0.247$ ($n_1 = 15$). In between these two lowest band edges is the energy range of our interest, which we depict as the *central region*. The n_0 th subband is the only propagating channel in the central region.

Expression for the dip structure behavior is presented below, as μ approaches the close vicinity of the n_1 th subband band edge from the central region side. We take $|\mu| = \varepsilon_{n_1,\min} - \Delta$, with $0 < \Delta \ll \varepsilon_{n_1,\min}$. From Eq. (B12), and assuming that the n_1 term in $G_{\mathcal{I}\mathcal{I}}$ is the dominating term, and that the $G_{\mathcal{I}\mathcal{I}}^2$ term in $\mathcal{D}(\mu, \mathcal{I})$ of Eq. (23) gives the dominating contribution, we get

$$\frac{1}{\tau_s^0} \approx \frac{\eta_M}{\hbar} \left[\frac{16J\beta_{n_1}}{T^2} \right]^2 \frac{(1 + \Delta h_{n_1})^2}{\sqrt{1 + \Delta h_{n_0}}} \times \sum_{M_i=0}^{W-1} \left[\frac{\varphi_{n_0}(i)}{\varphi_{n_1}^2(i)} \right]^4 \times \left[\frac{\Delta}{\varepsilon_{n_1,\min}} \right]^2. \quad (25)$$

Note that Eq. (25) is the limiting dip-structure behavior when μ is very close to the n_1 th subband band edge. The SRR suppression at a subband band edge is explicitly shown by the factor $(\Delta/\varepsilon_{n_1,\min})^2$ in Eq. (25). When μ moves away from $\varepsilon_{n_1,\min}$, or as Δ increases, we will need to include contributions from other subband terms in $G_{\mathcal{I}\mathcal{I}}$, and contributions from the other terms in $\mathcal{D}(\mu, \mathcal{I})$. As shown in Fig. 2, when μ increases towards $\varepsilon_{n_1,\min}$, the SRR develops a nice pre-dip profile before it reaches its limiting dip-structure behavior at the subband band edge. In other words, the overall

dip-structure profile covers a finite $\Delta\mu$ width. We stress that this nice profile causes the large suppression to remain intact at finite temperatures, and that it is originated from both the general trend of $G_{\mathcal{I}\mathcal{I}}$, to be discussed below, and sufficiently large values of α_0 and α_1 . That the large suppression results remain intact in finite temperatures is clearly shown in Fig. 1.

In addition, the overall profile of the SRR suppression characteristics remains intact even if the n_1 th subband transverse wave function $\varphi_{n_1}(j)$ has nodes. For $W = 98$, there is no node in $\varphi_{n_1}(j)$, while for $W = 20$ the nodes occur at $M_j = 6, 13$. The limiting SRR behavior when μ is very close to $\varepsilon_{n_1, \min}$ is then determined by these nodal sites, for the $W = 20$ case, given by

$$\frac{1}{\tau_s^0} \approx \frac{\eta_M}{2\hbar} (\alpha_1 - \alpha_0)^2 |\mu| \sum_{M_i=6,13} \frac{\xi(\mu, \mathcal{I})}{|\mathcal{D}(\mu, \mathcal{I})|^2}. \quad (26)$$

Since the singular n_1 term in $G_{\mathcal{I}\mathcal{I}}$ becomes zero when M_i is a node of the n_1 th subband transverse wave function, we return to the original expression for $1/\tau_s^0$ in Eq. (23), but keeping only the nodal M_i terms. It is because the non-nodal M_i terms in Eq. (23) follow the Eq. (25) behavior and thus do not contribute to Eq. (26). We note that even though the limiting SRR value, in Eq. (26), is not zero at the subband band edge, the overall profile of the SRR suppression characteristics should still remain intact. First, we can draw support from Fig. 2. That the overall profiles of the SRR suppression characteristics near $\varepsilon_{n_1, \min}$ consist of a finite $\Delta\mu$ width for the $W = 98$ and $W = 20$ curves provides a strong evidence. Second, we can also draw support from a general trend of $G_{\mathcal{I}\mathcal{I}}$. All the nonpropagating subband terms in $G_{\mathcal{I}\mathcal{I}}$, including the n_1 term, contribute constructively to give the general trend that the magnitude of $G_{\mathcal{I}\mathcal{I}}$ is increasing as μ increases towards $\varepsilon_{n_1, \min}$. Thus the vanishing of the n_1 term in $G_{\mathcal{I}\mathcal{I}}$ for a nodal M_i could not have changed this general trend in $G_{\mathcal{I}\mathcal{I}}$.

The major SRR peaks in Fig. 2, and within the central region, can be used to reveal its resonance nature. For the $W = 98$ case, the major SRR peak energies, indicated by the two arrows, are at -0.029 and 0.015 . These energies are matched by the analytic expression in Eq. (15), and after averaging over the transverse site M_i , to give $E_{R,0}^0 = -0.032$ and $E_{R,1}^0 = 0.017$. With this we see that the resonance nature of the $W = 98$ major SRR peaks are j -resolved resonances.

For the $W = 20$ case, the $E_{R,j}^0$ calculation does not produce a good match in the major SRR peak energies. Using Eq. (17) instead, where we determine the energies $E_{R,\pm}$ numerically, and after averaging over M_i , we get $E_{R,-} = -0.048$ and $E_{R,+} = 0.037$. The corresponding major SRR peak energies in Fig. 2 are -0.043 and 0.037 . This excellent matching shows unequivocally the j -mixed resonance nature of the major SRR peaks.

We may note in passing the at-the-resonance behavior of the spin-flipped transmission and reflection coefficients. From Eq. (19), taking the resonance at, say, $E_{R,j}^0$, the factor $(\alpha_1 - \alpha_0)^2 / |\mathcal{D}(\mu, \mathcal{I})|^2 \approx 1 / (\text{Im } G_{\mathcal{I}\mathcal{I}})^2$. Also, taking the $n' = n = n_0$ condition, because we are referring to the central region, we obtain

$$|r_{n_0 n_0}^f(\bar{S}, S)|^2 = |t_{n_0 n_0}^f(\bar{S}, S)|^2 \cong \frac{1}{4}. \quad (27)$$

From this result, we have the spin-flipped current, both reflection and transmission included, given by $v_{g_{n_0}}(\mu) / (N_y 2\sqrt{3} a)$. This is actually one half of the incident current, namely, $v_{g_{n_0}}(\mu) / (N_y \sqrt{3} a)$. In other words, the spin-flipped outgoing current is the same as the non-spin-flipped outgoing current, and the spin has then reached an unpolarized outgoing state at the resonance. Similar at-the-resonance behavior of a MI was found in graphene [29]. This happens when the initial spin configurations are $|\uparrow\downarrow\rangle$ or $|\downarrow\uparrow\rangle$. The electron experiences no spin-flip for the initial spin configurations $|\uparrow\uparrow\rangle$ or $|\downarrow\downarrow\rangle$.

III. COHERENT EFFECTS FROM MANY MAGNETIC IMPURITIES

This section presents the many magnetic impurity scattering treatment. Analytic analysis for the case of two MIs is performed to reveal the physics behind many MI effects on the two SRR suppressions, at a subband band edge and at the MI resonance. Comparison with numerical examples presents a quantitative confirmation of the SRR suppression at the MI resonance. We also present numerical results for a systematic increasing of the number of magnetic impurities involved in the multiple scattering. Both the robustness of the SRR suppression at a subband band edge, and the trend of the suppression of the SRR at the MI resonance are demonstrated.

Multiple scattering of a conduction electron by \mathcal{N}_M magnetic impurities in the AGNRs is formulated in the following to exhibit the structures in the scattering state. Extending \hat{H}_{ad} in Eq. (3) to this case, and we have \hat{V}_{ad} given by

$$\hat{V}_{ad} = \sum_{\mathcal{I}, v} |\mathcal{I}\rangle \langle \mathcal{I}| \otimes \left[\sum_{u_{\mathcal{I}}} V_{v, u_{\mathcal{I}}}^{\text{nf}} |v, u_{\mathcal{I}}\rangle \langle v, u_{\mathcal{I}}| + \sum_{u_{\mathcal{I}} \neq v} V_0^f |\bar{v}, \bar{u}_{\mathcal{I}}\rangle \langle v, u_{\mathcal{I}}| \right], \quad (28)$$

where a specific \mathcal{K} th realization of the spin configuration $\mathbb{S}_{\mathcal{K}}$ is given by $\mathbb{S}_{\mathcal{K}} = (v_{\mathcal{K}}; u_{1\mathcal{K}}, u_{2\mathcal{K}}, \dots, u_{\mathcal{I}\mathcal{K}}, \dots, u_{\mathcal{N}_M\mathcal{K}})$. We also have defined functions $v_{\mathcal{K}} = v(\mathbb{S}_{\mathcal{K}})$ and $u_{\mathcal{I}\mathcal{K}} = u_{\mathcal{I}}(\mathbb{S}_{\mathcal{K}})$ to extract the components of the system spin configuration $\mathbb{S}_{\mathcal{K}}$.

The scattering state $|\Psi_{\mathbf{k}_n}; \mathbb{S}_{in}\rangle$ resulted from the incident state $|\psi_{\mathbf{k}_n}; \mathbb{S}_{in}\rangle$ is given by

$$|\Psi_{\mathbf{k}_n}; \mathbb{S}_{in}\rangle = \sum_{\mathcal{K}}' |\Psi_{\mathbf{k}_n, \mathbb{S}_{in}}^{\mathcal{S}_{\mathcal{K}}}\rangle \otimes |\mathcal{S}_{\mathcal{K}}\rangle, \quad (29)$$

where the primed summation denotes spin configurations $\mathbb{S}_{\mathcal{K}}$ of which its total spin along z , given by $M_{z, \mathcal{K}} = \frac{\hbar}{2}(v_{\mathcal{K}} + \sum_{\mathcal{I}} u_{\mathcal{I}\mathcal{K}})$ is the same as that of \mathbb{S}_{in} . Substituting Eq. (29) into the Lippmann-Schwinger equation

$$|\Psi_{\mathbf{k}_n}; \mathbb{S}_{in}\rangle = |\psi_{\mathbf{k}_n}; \mathbb{S}_{in}\rangle + \hat{G}\hat{V}_{ad} |\Psi_{\mathbf{k}_n}; \mathbb{S}_{in}\rangle, \quad (30)$$

and projecting onto $\langle \mathcal{I}| \otimes \langle \mathcal{S}_{\mathcal{K}}|$, at the location of an magnetic impurity, gives

$$\begin{aligned} \Psi_{\mathbf{k}_n, \mathbb{S}_{in}}^{\mathcal{S}_{\mathcal{K}}}(\mathcal{I}) &= \delta_{in, \mathcal{K}} \psi_{\mathbf{k}_n}(\mathcal{I}) + \sum_{\mathcal{I}'} G_{\mathcal{I}\mathcal{I}'} V_{v, u_{\mathcal{I}'}}^{\text{nf}}(\mathcal{S}_{\mathcal{K}}) \Psi_{\mathbf{k}_n, \mathbb{S}_{in}}^{\mathcal{S}_{\mathcal{K}}}(\mathcal{I}') \\ &+ \sum_{\mathcal{I}'} \sum_{\mathcal{K}'} G_{\mathcal{I}\mathcal{I}'} V_0^f \langle \mathcal{S}_{\mathcal{K}} | \mathcal{F}_{\mathcal{I}'} | \mathcal{S}_{\mathcal{K}'} \rangle \Psi_{\mathbf{k}_n, \mathbb{S}_{in}}^{\mathcal{S}_{\mathcal{K}'}}(\mathcal{I}'), \end{aligned} \quad (31)$$

where the primed summation has excluded the $\mathcal{K}' = \mathcal{K}$ case.

The two subscripts of $V_{\nu u_{\mathcal{I}}}^{\text{nf}}(\mathcal{S}_{\mathcal{K}})$ in the second term of Eq. (31), namely, ν and $u_{\mathcal{I}}$, are the values of $\nu(\mathcal{S}_{\mathcal{K}})$ and $u_{\mathcal{I}}(\mathcal{S}_{\mathcal{K}})$, respectively. The spin configuration $\mathcal{F}_{\mathcal{I}}[\mathcal{S}_{\mathcal{K}}]$ is defined as

$$\mathcal{F}_{\mathcal{I}}[\mathcal{S}_{\mathcal{K}}] = \begin{cases} 0 & \text{if } \nu_{\mathcal{K}} = u_{\mathcal{I}\mathcal{K}}, \\ (\bar{\nu}_{\mathcal{K}}; u_{1\mathcal{K}}, \dots, \bar{u}_{\mathcal{I}\mathcal{K}}, \dots, u_{N_{\text{M}}\mathcal{K}}) & \text{if } \nu_{\mathcal{K}} = \bar{u}_{\mathcal{I}\mathcal{K}}, \end{cases} \quad (32)$$

which is flipping the electron spin and the local moment at \mathcal{I} if they are antiparallel with each other.

Solving the set of equations given by Eq. (31) determines the scattering state at the locations of all the MIs. These results can be used to calculate the scattering state at an arbitrary site $|\mathcal{J}\rangle$, and from it we can extract the spin-flipped transmission and reflection coefficients as well as the spin-relaxation rate, according to the method illustrated in Sec. II A.

A. Case of two magnetic impurities

In this section, we present an analytic electron multiple scattering calculation involving two MIs and for a specific incident system-spin configuration. The incident system-spin configuration we consider here is $|\downarrow\uparrow\uparrow\rangle$ (labeled as $|a\rangle$ below for simplicity), and the other system-spin configurations involved are $|\uparrow\downarrow\uparrow\rangle$ (labeled as $|b\rangle$) and $|\uparrow\uparrow\downarrow\rangle$ (labeled as $|c\rangle$). We will present that the near subband band edge behavior remain intact in this analysis.

For an incident state $|\psi_a\rangle \otimes |a\rangle$, where the incident subband n_0 and wave vector \mathbf{k}_{n_0} have been kept implicit, and following Eq. (31), we get

$$\begin{aligned} \mathbf{M}_1 \tilde{\Psi}(1) + \Gamma \tilde{\Psi}(2) &= \mathbf{A}, \\ \Gamma \tilde{\Psi}(1) + \mathbf{M}_2 \tilde{\Psi}(2) &= \mathbf{B}, \end{aligned} \quad (33)$$

where

$$\mathbf{M}_1 = \begin{pmatrix} G_{11}V_0^{\text{nf}} - 1 & G_{11}V_0^{\text{f}} & 0 \\ G_{11}V_0^{\text{f}} & G_{11}V_0^{\text{nf}} - 1 & 0 \\ 0 & 0 & G_{11}V_1^{\text{nf}} - 1 \end{pmatrix}, \quad (34)$$

$$\Gamma = G_{12} \begin{pmatrix} V_0^{\text{nf}} & V_0^{\text{f}} & 0 \\ 0 & 0 & V_1^{\text{nf}} \\ V_0^{\text{f}} & V_0^{\text{nf}} & 0 \end{pmatrix}, \quad (35)$$

$$\mathbf{A} = \begin{pmatrix} -\psi_a(1) \\ 0 \\ 0 \end{pmatrix}, \quad \mathbf{B} = \begin{pmatrix} -\psi_a(2) \\ 0 \\ 0 \end{pmatrix}, \quad (36)$$

and

$$\tilde{\Psi}(1) = \begin{pmatrix} \Psi_a(1) \\ \Psi_b(1) \\ \Psi_c(1) \end{pmatrix}, \quad \tilde{\Psi}(2) = \begin{pmatrix} \Psi_a(2) \\ \Psi_c(2) \\ \Psi_b(2) \end{pmatrix}. \quad (37)$$

The matrix \mathbf{M}_2 is obtained from Eq. (34) by replacing the coordinate from \mathcal{I}_1 to \mathcal{I}_2 . In this analytic analysis, the two MIs are chosen to locate on the same-site type. Our numerical calculations, however, are not limited to the same-site-type case.

To facilitate the comparison with independent MI effects, we introduce the independent MI scattering solutions $\tilde{\Psi}^{(0)}$. These are the solutions to Eq. (33), when Γ is set to zero, and are given by

$$\tilde{\Psi}^{(0)}(1) = \mathbf{M}_1^{-1}\mathbf{A}, \quad \text{and} \quad \tilde{\Psi}^{(0)}(2) = \mathbf{M}_2^{-1}\mathbf{B}. \quad (38)$$

We obtain

$$\begin{aligned} \tilde{\Psi}(1) &= [1 - (\mathbf{M}_1^{-1}\Gamma\mathbf{M}_2^{-1}\Gamma)]^{-1} \tilde{\Psi}^{(0)}(1) \\ &\quad - \mathbf{M}_1^{-1}\Gamma[1 - (\mathbf{M}_2^{-1}\Gamma\mathbf{M}_1^{-1}\Gamma)]^{-1} \tilde{\Psi}^{(0)}(2). \end{aligned} \quad (39)$$

Again, the expression for $\tilde{\Psi}(2)$ is obtained from Eq. (39) by interchanging coordinates $\mathcal{I}_1 \leftrightarrow \mathcal{I}_2$.

We simplify Eq. (39) by choosing the two MIs to have the same transverse site location. Then $\mathbf{M}_1 = \mathbf{M}_2$, and we have

$$\begin{aligned} \tilde{\Psi}(1) &= [1 - (\mathbf{M}_1^{-1}\Gamma\mathbf{M}_1^{-1}\Gamma)]^{-1} \\ &\quad \times [\tilde{\Psi}^{(0)}(1) - \mathbf{M}_1^{-1}\Gamma\tilde{\Psi}^{(0)}(2)], \end{aligned} \quad (40)$$

where $\tilde{\Psi}(1)$ carries a suppression factor $G_{\mathcal{I}\mathcal{I}}^{-1}$ when μ is in the close vicinity of a subband band edge, as is evident from Eq. (38).

The robustness of the SRR suppression at a subband band edge is illustrated in Fig. 3, where results for independent MIs (red curve) and for incoherent MI clusters (black curve) are presented for comparison. The MI cluster considered here has two MIs per cluster. As shown are the central region for μ , AGNRs with $W = 98$, and MI fraction $\eta_{\text{M}} = 10^{-6}$. The overlapping of the two curves over a large portion of the central region, including the n_1 th subband band edge, provides a strong indication of the robustness of our SRR suppression results. The deviation between the two curves occurs in the MI resonance region, indicated by the arrows. This will be discussed in the next section. Before we present our discussion

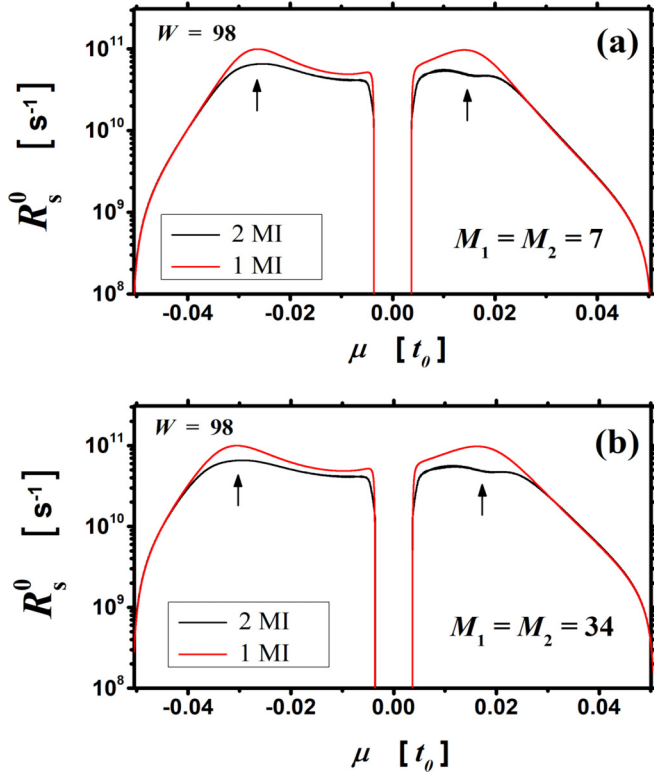


FIG. 3. Zero-temperature SRR R_s^0 vs chemical potential μ for independent MI (red curves) and for incoherent MI-cluster (black curve, 2 MI per cluster) results. The R_s^0 , given by Eq. (41), contains specific configurations. For the independent MI case, the specific configuration is the transverse-site location $M = 7$ in (a), and 34 in (b), respectively. Specific configurations for the incoherent MI-cluster case are the transverse-site locations $M_1 = M_2 = 7$ in (a) and 34 in (b). Average over the longitudinal MI-separation L_{21} includes all cases within a range $0 \leq L_{21} \leq 3000$ for the incoherent MI cluster case. Incident spin-configuration averaging has been performed for all the curves. Depicted by arrows are the R_s^0 suppression, of the incoherent MI-cluster results relative to the independent MI results, at the resonance. The magnetic impurity fraction $\eta_M = 10^{-6}$. To make connection with previous figures, R_s^0 has included a factor $\mathcal{N}_M/\mathcal{N}_{\text{coh}}$, where $\mathcal{N}_{\text{coh}} = 1(2)$ for independent MIs (two-MI clusters).

on the SRR suppression physics associated with the subband band edge, an account on our averaging scheme is presented below. The R_s^0 plotted in Fig. 3 has included a numerical factor $\mathcal{N}_M/\mathcal{N}_{\text{coh}}$ so as to give the relevant orders of magnitude as in the previous figures. Explicitly, this R_s^0 is given by

$$R_s^0 = \frac{\mathcal{N}_M}{\mathcal{N}_{\text{coh}}} \frac{1}{\mathcal{N}_S} \sum_S \left\langle \sum_{S'} R_s^0(n_0, S'; S) \right\rangle_L, \quad (41)$$

where $\mathcal{N}_{\text{coh}} = 1(2)$ for independent MIs (incoherent two-MI clusters), and the subscripted configuration average $\langle \dots \rangle_L$ denotes averaging over longitudinal coordinates.

Averaging in Eq. (41) over all the incident spin configurations S has the number of spin configurations $\mathcal{N}_S = 4$ ($\mathcal{N}_S = 8$) for the independent MI (incoherent MI cluster) case. Only final spin configurations S' that have its electron spin flipped related to S will be included. The transverse MI site locations in Eq. (41), however, are kept fixed, with $M_1 = M_2 = 7$ in

Fig. 3(a), and $M_1 = M_2 = 34$ in Fig. 3(b). This allows us to make a closer comparison with our analytical results for the SRR suppression at a MI resonance in the next section.

Averaging in Eq. (41) of the longitudinal coordinates is over the MI-separation $L_{21} \equiv N_2 - N_1$ for the incoherent MI-cluster case. The ensemble includes all L_{21} cases within a range $0 \leq L_{21} \leq 3000$. We note that the typical L_{21} associated with η_M between two MIs is $\Delta N_\eta = 1/(\eta_M W) \sim 10^4$, which is a bit larger than, but within the same order of magnitude as, our choice of the upper limit for the L_{21} . Meanwhile the incoherent MI-cluster results are found to have already reached the same averaged R_s^0 curve in Fig. 3 as early as when the upper limit of the L_{21} equals 500. Thus our choice of the ensemble for the L_{21} average is reasonable. We further note that the curves in Fig. 3 are smooth. This is an indication that we have invoked a large L_{21} ensemble for the L_{12} -ensemble average of the R_s^0 . As for the independent MI case, no longitudinal coordinate averaging is needed.

The overlapping of the independent MI and the incoherent MI-cluster curves (Fig. 3) covers over a half of the central region, extending from the n_1 th subband band edge. It is very interesting and deserves an in depth discussion. Looking at individual L_{12} -specified cases (not shown) chosen from among the L_{12} ensemble, all the R_s^0 exhibit the SRR suppression in the vicinity of the n_1 th subband band edge. Meanwhile, for a sufficiently large L_{21} , the overlapping resembles that in Fig. 3. Hence we call this overlapping region the nonresonance region. When L_{21} is not large enough, deviation occurs in the nonresonance region between the incoherent MI-cluster and the independent MI curves. However, this deviation is different in its physical nature to the deviation in the remaining part of the central region. We call this remaining part of the central region, including the lower $|\mu|$ part, $\varepsilon_{n_0, \text{min}}$ and the MI resonance energies, the resonance region. In the resonance region, apparent deviations, with rapid fluctuations, occur between the independent MI and the incoherent MI-cluster curves. In the nonresonance region, deviations occur for $L_{21} \lesssim 100$, while the incoherent MI-cluster curves fall on top of the independent MI curves for $L_{21} \gtrsim 100$. This shows that a L_{12} -ensemble average of the R_s^0 up to the upper L_{12} limit of 3000 would have largely diminished, in the nonresonance region, the deviation between the independent MI and the incoherent MI-cluster curves. On the other hand, in the resonance region, the deviation between the two curves is not removed by the L_{12} averaging, except for the fluctuations. Further discussion of the resonance region will be presented in the next section.

Presented below is our explanation for the above observed fact that, in the nonresonance region, the L_{21} -specified R_s^0 from incoherent MI-cluster calculations matches nicely with the independent MIs results when L_{21} is large enough. It is directly related to the contributions to $G_{21}(\mu)$ and $G_{11}(\mu)$ from the $n \neq n_0$ subbands. We add that these are the nonpropagating subbands and they contribute only to the real part of the Green's functions. Consider the situation when contribution from $n \neq n_0$ subbands to $G_{21}(\mu)$ can be neglected, for large enough L_{21} [see Eq. (B10)], but the corresponding contribution to $G_{11}(\mu)$ is significant. Then the Green's function ratio $|G_{21}(\mu)/G_{11}(\mu)|$ is smaller than unity. Contributions of the n_0 th subband to $G_{21}(\mu)$ and $G_{11}(\mu)$ have the same magnitude,

though they are complex and pure imaginary, respectively [see Eq. (B9)].

We find out that (not shown) the Green's function ratio $|G_{21}(\mu)/G_{11}(\mu)| \leq 0.3$ in the nonresonance region when $L_{21} \geq 100$. This Green's function ratio is reckoned to be the key factor in $\mathbf{M}_1^{-1}\mathbf{\Gamma}$ that represents, in the nonresonance region, the significance of communications between the two MIs in setting up the scattering wave function [see Eq. (40)]. Deviation between the two curves is given by, in the leading order, the above Green's function ratio squared. Summarizing all we get above for the nonresonance region, the physical picture is that, when the Green's function ratio is small for an inter-MI longitudinal separation L_{21} , the inter-MI communication will become unimportant so that the R_s^0 will exhibit independent-MI characteristics.

As $|\mu|$ in the nonresonance region decreases, the aforementioned Green's function ratio increases, due to decreasing contributions from the $n \neq n_0$ subbands to $G_{11}(\mu)$. Meanwhile, as $|\mu|$ is getting closer to the MI resonance, the matrix elements in \mathbf{M}_1^{-1} increases. It is because of the $\mathcal{D}(\mu, \mathcal{I})^{-1}$ factor contained in the matrix elements, and that $\mathcal{D}(\mu, \mathcal{I})$ is decreasing. These two developments together drive the system from the nonresonance to the resonance region. The physical picture established above holds also for the case of $W = 20$. However, additional oscillatory deviation behavior occurs for $W = 20$ in the nonresonance region. It is due to the phase factor attaching to the n_0 th subband term in $G_{21}(\mu)$. It brings forth oscillatory behaviors, arising from the interference leading from the superposition in Eq. (40). A larger energy range for the central region, due to the smaller W , also contributes to the appearance of this oscillatory behavior. This oscillatory behavior depends on L_{21} , and is thus subjected to be eliminated by the L_{21} averaging.

We end this section by getting back to the smooth R_s^0 profile we have obtained in our L_{21} averaging from a large ensemble. This suggests us a $\Delta\mu$ -averaging scheme in place of a real-space L_{21} averaging. The scheme is to apply a small $\Delta\mu$ averaging to a L_{21} -specific R_s^0 of incoherent two-MI clusters. Indeed, we find out that (not shown here) the incoherent MI cluster results in Fig. 3 can be nicely reproduced by averaging a L_{21} -specific R_s^0 over μ within a $\Delta\mu = 0.001$ interval, with the L_{21} arbitrary chosen a value $L_{21} = 5000$. This is an impressive demonstration of the mesoscopic physics, where $\Delta\mu$ averaging plays the role of a configuration averaging [65]. We will use this $\Delta\mu$ -averaging scheme in place of the real-space L_{21} -averaging for clusters consisting of larger number of MIs.

B. Suppression of SRR at resonance: case of two magnetic impurities

In this section, we demonstrate the SRR suppression due to MI resonance by deriving the SRR R_s^0 expression at the MI resonance energies $\mu = E_{R,j}^0$. The resonance energies are depicted by arrows in Fig. 3. Specifically, the suppression will be given by the proportionality factor connecting the R_s^0 for incoherent two-MI clusters and for independent MIs. The μ range of our interest is the central region.

Our derivation is based on a resonance approximation hinted by the form of the matrix elements in \mathbf{M}_1^{-1} . The nonzero matrix elements of \mathbf{M}_1^{-1} , derived from

Eq. (34), are $(\mathbf{M}_1^{-1})_{11} = (\mathbf{M}_1^{-1})_{22} = -\frac{1}{2}[\frac{1}{1-\alpha_0 G_{11}} + \frac{1}{1-\alpha_1 G_{11}}]$, $(\mathbf{M}_1^{-1})_{12} = (\mathbf{M}_1^{-1})_{21} = \frac{1}{2}[\frac{1}{1-\alpha_0 G_{11}} - \frac{1}{1-\alpha_1 G_{11}}]$, and $(\mathbf{M}_1^{-1})_{33} = -\frac{1}{1-\alpha_1 G_{11}}$. These are in the form readied for MI resonances at $E_{s,j}^0$.

Consider $\mu = E_{R,0}^0$ in the following. Our resonance approximation scheme is to drop all $\frac{1}{1-\alpha_1 G_{11}}$ terms in \mathbf{M}_1^{-1} to give

$$\mathbf{M}_1^{-1} \approx \frac{-1}{2(1-\alpha_0 G_{11})} \begin{pmatrix} 1 & -1 & 0 \\ -1 & 1 & 0 \\ 0 & 0 & 0 \end{pmatrix}. \quad (42)$$

Following on the consideration in the previous section, Eqs. (42) and (38) lead to $\tilde{\Psi}^{(0)}$ having only two components, namely, $|a\rangle$ and $|b\rangle$ at the location of the first MI (MI-1), and $|a\rangle$ and $|c\rangle$ at the location of the MI-2. We note that the two components of $\tilde{\Psi}^{(0)}$ at a MI site correctly reflects the symmetry form expected for the $E_{R,0}^0$ resonance, as is discussed in the paragraph after Eq. (16). Also, we take the condition $|E_{R,0}^0| \ll \varepsilon_{n_1, \min}$ for our analysis below. We thus obtain

$$\mathbf{M}_1^{-1} \mathbf{\Gamma} \tilde{\Psi}^{(0)}(1) \approx \lambda_0 \alpha_0 \tilde{\Psi}^{(0)}(1), \quad (43)$$

where $\lambda_0 \alpha_0 = \frac{-G_{12} \alpha_0}{2(1-\alpha_0 G_{11})} \approx \frac{1}{2} e^{i\gamma} Q_{n_0} |L_{12}|$. Finally, from Eq. (39) and from the fact that $\tilde{\Psi}^{(0)}(2)$ also satisfies Eq. (43), we arrive at the important relation for $\tilde{\Psi}(1)$, given by

$$\tilde{\Psi}(1) \approx \frac{1}{1 - \lambda_0^2 \alpha_0^2} [\tilde{\Psi}^{(0)}(1) - \lambda_0 \alpha_0 \tilde{\Psi}^{(0)}(2)]. \quad (44)$$

$\tilde{\Psi}(2)$ is obtained when $\mathcal{I}_1 \leftrightarrow \mathcal{I}_2$ is performed in Eq. (44).

Before we obtain the spin-flipped transmission and reflection coefficients from Eq. (44), it is convenient to first obtain the independent impurity results. Our method follows that presented in Sec. II A. The spin-flipped coefficient $t_{n_0 n_0}^{f(0)}(b, a; 1)$ from an independent MI-1, which connects only to the $|b\rangle$ state in the outgoing wave, is more conveniently expressed in a form involving $\tilde{\Psi}^{(0)}(1)$, rather than in the form given in Eq. (18). Here we introduce the superscript (0) in $t_{n_0 n_0}^{f(0)}(b, a; 1)$ to stress its independent MI nature, and to separate from the spin-flipped coefficients for the two-MI case below. The spin-flipped transmission coefficient for the independent MIs is given by

$$t_{n_0 n_0}^{f(0)}(b, a; 1) = -i \sqrt{\frac{N_y}{2(1 + \Delta h_{n_0})}} e^{-i\gamma Q_{n_0} N_1} \varphi_{n_0}(1) \times [V_0^{\text{nf}} \Psi_b^{(0)}(1) + V_0^f \Psi_a^{(0)}(1)]. \quad (45)$$

Similarly, one can show that

$$r_{n_0 n_0}^{f(0)}(b, a; 1) = t_{n_0 n_0}^{f(0)}(b, a; 1) e^{2i\gamma Q_{n_0} N_1}, \quad (46)$$

and $t_{n_0 n_0}^{f(0)}(b, a; 1) = t_{n_0 n_0}^{f(0)}(c, a; 2)$, when $M_1 = M_2$.

Now, we turn to the incoherent two-MI cluster results. To extract the spin-flipped transmission and reflection coefficients arising from MI-1, we consider projecting the spin-flipped outgoing wave at an arbitrary site $|\mathcal{J}\rangle$ to give $\Psi_b(\mathcal{J}) = G_{\mathcal{J}1} [V_0^{\text{nf}} \Psi_b(1) + V_0^f \Psi_a(1)]$. From this projection

expression, and together with Eq. (44), we obtain

$$t_{n_0 n_0}^f(b, a; 1) = \frac{1 - \frac{1}{2} e^{i\gamma Q_{n_0} (|L_{12}| - L_{12})}}{1 - \frac{1}{4} e^{2i\gamma Q_{n_0} |L_{12}|}} t_{n_0 n_0}^{f(0)}(b, a; 1). \quad (47)$$

Similarly, one can obtain

$$t_{n_0 n_0}^f(c, a; 2) = \frac{1 - \frac{1}{2} e^{i\gamma Q_{n_0} (|L_{12}| + L_{12})}}{1 - \frac{1}{4} e^{2i\gamma Q_{n_0} |L_{12}|}} t_{n_0 n_0}^{f(0)}(b, a; 1). \quad (48)$$

The reflection coefficients $r_{n_0 n_0}^f(b, a; 1)$ and $r_{n_0 n_0}^f(c, a; 2)$ bear the same relation form with $t_{n_0 n_0}^f(b, a; 1)$ and $t_{n_0 n_0}^f(c, a; 2)$, respectively, as that given in Eq. (46). Only that the location N_1 in the phase factor on the right-hand side of Eq. (46) should be changed to N_2 if the relation is applied to MI-2.

It is of interest to see that the spin-flipped outgoing waves from MI-1 do not interfere with that emanating from MI-2, because of different spin configurations in $|b\rangle$ and $|c\rangle$. We note that this is in sharp contrast with normal scatterer, where all outgoing scattered waves, which would be non-spin-flip only, of the same energy will certainly interfere and will lead to deviation from independent-scatterer results. Thus the MIs would be easier to establish independent MIs characteristics than normal scatterers.

The zero-temperature total spin-relaxation rate $R_s^0(n_0, a)$ for the incident state $|\psi_a\rangle \otimes |a\rangle$ at the resonance energy $E_{R,0}^0$, follow Eq. (A11), is given by

$$R_s^0(n_0, a) = \frac{\mathcal{N}_M}{\mathcal{N}_{\text{coh}} N_y \sqrt{3} a} \sum_{\alpha=1}^2 \left[|t_{n_0 n_0}^f(S', a; \alpha)|^2 + |r_{n_0 n_0}^f(S', a; \alpha)|^2 \right], \quad (49)$$

where the primed summation denotes $S' = b$ and c for, respectively, $\alpha = 1$ and 2. The factor $\mathcal{N}_M/\mathcal{N}_{\text{coh}}$ has been introduced to Eq. (49) for Fig. 3, in order to give the relevant orders of magnitude as in Figs. 1 and 2. Here $\mathcal{N}_{\text{coh}} = 2$.

For comparison, the independent MI results for the corresponding total spin-relaxation rate $R_s^{\text{Ind}}(n_0, a)$ is given by

$$R_s^{\text{Ind}}(n_0, a) = \mathcal{N}_M \frac{4v_{\text{gn}_0}}{N_y \sqrt{3} a} |t_{n_0 n_0}^{f(0)}(b, a; 1)|^2. \quad (50)$$

Again, the prefactor \mathcal{N}_M has been added to accommodate the total contribution from the MIs in Fig. 3.

The important relation between $R_s^0(n_0, a)$ and $R_s^{\text{Ind}}(n_0, a)$, for the case of $N_2 > N_1$, and at $\mu = E_{R,0}^0$, is then obtained

$$R_s^0(n_0, a) = \frac{A_0 + 1/4}{A_0 + 9/16} R_s^{\text{Ind}}(n_0, a) \quad (51)$$

where $A_0 = \sin^2(Q_{n_0} L_{21})$. The expression clearly shows the suppression of the spin-relaxation rate at the resonance energy $E_{R,0}^0$.

However, the two-MI cluster SRR R_s^0 shown in Fig. 3 has been averaged over incident spin configurations and over L_{21} , while keeping $M_1 = M_2$ at fixed values. So, to perform the incident spin-configuration average, we need to also calculate $R_s^0(n_0, \bar{b})$, $R_s^0(n_0, \bar{c})$ and $R_s^0(n_0, d)$. Here $|\bar{b}\rangle$ is the spin state with all the spins in $|b\rangle$ reversed, and $|d\rangle = |\downarrow\downarrow\downarrow\rangle$ has zero spin-flipping rate. Similar to the method leading to Eq. (51), we get $R_s(n_0, \bar{b}) = R_s(n_0, \bar{c}) = \frac{1}{2} R_s(n_0, a)$. The

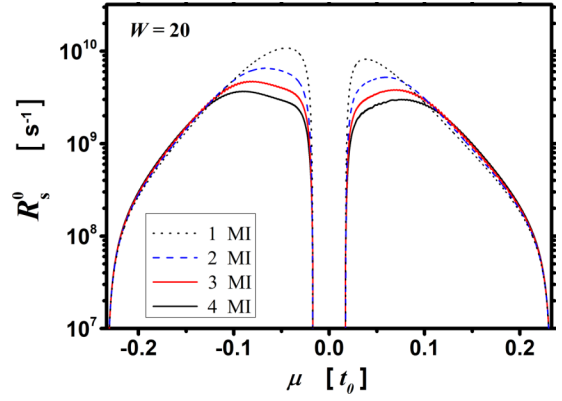


FIG. 4. Zero-temperature SRR R_s^0 vs chemical potential μ for incoherent MI-cluster results. The number of MI in a cluster equals 1 (black dotted), 2 (blue dashed), 3 (red solid), and 4 (black solid), with incident spin configurations given, respectively, by $|\downarrow\uparrow\rangle$, $|\downarrow\uparrow\uparrow\rangle$, $|\downarrow\uparrow\uparrow\uparrow\rangle$, and $|\downarrow\uparrow\uparrow\uparrow\uparrow\rangle$. All transverse site locations are fixed at $M = 7$. R_s^0 is basically given by Eq. (41) except that there is no incident spin configuration averaging. The magnetic impurity fraction $\eta_M = 10^{-6}$.

spin and L_{21} averaged R_s^0 shown in Fig. 3 is given by $R_s^0 = \frac{1}{2} (R_s^0(n_0, a))_{L_{21}}$, whereas the spin-configuration averaged independent-MI SRR is denoted by $R_s^{\text{Ind}} = \frac{1}{2} R_s^{\text{Ind}}(n_0, a)$. Finally, we obtain the important relation between the two curves in Fig. 3 at the MI resonance energy $E_{R,0}^0$, given by

$$R_s^0 = \left\langle \frac{A_0 + 1/4}{A_0 + 9/16} \right\rangle_{L_{21}} R_s^{\text{Ind}}. \quad (52)$$

Excellent matching of the ratio R_s^0/R_s^{Ind} obtained from Fig. 3 and from Eq. (52) is presented below. For Fig. 3(a), when $M_1 = M_2 = 7$, the ratio from the figure [Eq. (52)] is 0.66 (0.67). The R_s^0/R_s^{Ind} ratios in Fig. 3(b), when $M_1 = M_2 = 34$, are the same as that in Fig. 3(a).

At the resonance energy $E_{R,1}^0$, similar analysis gives us

$$R_s^0 = \left\langle \frac{20A_0}{16A_0 + 9} \right\rangle_{L_{21}} R_s^{\text{Ind}}. \quad (53)$$

This expression also agrees very well with our numerical results. In Fig. 3(a), the ratio from the figure [Eq. (53)] is 0.51 (0.50). The corresponding ratios in Fig. 3(b) are the same as that in Fig. 3(a).

C. Incoherent MI cluster

In this section, we present incoherent MI-cluster results, when the number (\mathcal{N}_{coh}) of MIs in a cluster increases sequentially, from $\mathcal{N}_{\text{coh}} = 1$ up to $\mathcal{N}_{\text{coh}} = 4$. The trends, shown in Fig. 4, exhibit in the SRR R_s^0 are the robustness of the SRR suppression in the nonresonance region and the suppression characteristics of the SRR in the resonance region.

The zero-temperature SRR R_s^0 shown in Fig. 4 has been averaged over the MIs' longitudinal separations, while all the transverse site locations are fixed, at $M = 7$, and incident spin configurations are specified. The R_s^0 is basically given by Eq. (41) except that there is no incident spin configuration

averaging. In the order of increasing \mathcal{N}_{coh} , the incident spin configurations are $|\downarrow\uparrow\rangle$, $|\downarrow\uparrow\uparrow\rangle$, $|\downarrow\uparrow\uparrow\uparrow\rangle$, and $|\downarrow\uparrow\uparrow\uparrow\uparrow\rangle$, respectively. This choice of the incident spin configuration should be a good representation for each \mathcal{N}_{coh} to reveal the trend of the variation of the SRR characteristics as \mathcal{N}_{coh} increases. On the other hand, a full incident spin configuration average has been performed for our finite temperature SRR $1/\tau_s$ result, presented in Fig. 1, for the incoherent three-MI cluster ($\mathcal{N}_s = 3$) case. The magnetic impurity fraction $\eta_M = 10^{-6}$ is the same for all curves.

Two longitudinal separation averaging schemes have been invoked in Fig. 4. A real-space averaging has been applied to the $\mathcal{N}_{\text{coh}} = 2$ curve, with a L_{21} ensemble including all L_{21} within the interval $0 \leq L_{21} \leq 5000$. For the $\mathcal{N}_{\text{coh}} = 3$, and 4 curves, a $\Delta\mu$ -averaging scheme, as is discussed in section III A, has been used. In the $\mathcal{N}_{\text{coh}} = 3$ curve, we have averaged R_s^0 over μ by a $\Delta\mu = 0.0018$ interval. The choice for the longitudinal separations between the three MIs, chosen to be $L_{21} = 5000$ and $L_{32} = 7000$ for Fig. 4, is found not crucial to the R_s^0 curve. Here MIs are labeled in order of their longitudinal positions. We recall that the typical longitudinal separation between two MIs is given by $\Delta N_\eta = 1/(\eta_M W) \sim 5 \times 10^4$ for the case of $W = 20$ in Fig. 4. Our finding that the above $\Delta\mu$ -averaging scheme gives the same R_s^0 curve as long as the above longitudinal separations are greater than 10^3 , which is a reasonable range of choices from the ΔN_η perspective, is a strong assurance of the validity of our $\Delta\mu$ -averaging scheme. Even if the longitudinal separation goes down to 500, the same R_s^0 curve can still be obtained if we slightly increase $\Delta\mu$ to 0.004 for the averaging. Similarly, the $\mathcal{N}_{\text{coh}} = 4$ curve has used the same $\Delta\mu$ -averaging scheme with $\Delta\mu = 0.0018$, $L_{21} = 5000$, $L_{32} = 7000$, and $L_{43} = 9000$.

In Fig. 4, we can see the remarkable overlapping of the four curves not only near the n_1 th subband band edge, but also extends from there to cover more than one half of the central region. This is a clear demonstration of the robustness of the SRR suppression features. The region of interest here is the nonresonance region pointed out in Sec. III A. Discussions in Sec. III A has shown, for the case of incoherent two-MI clusters, two physical reasons that helped uphold the nice overlapping finding. These are the singular feature of $G_{II}(\mu)$, at the subband band edge, and the role of small $|G_{12}(\mu)/G_{11}(\mu)|$ as to impose a μ dependent finite range of communication, via the electrons, between the MIs. The overlapping findings here for $\mathcal{N}_{\text{coh}} > 2$ cases show that the same two physical reasons remain at work for incoherent multi-MI clusters.

The SRR suppression characteristics in the resonance region has shown, in Fig. 4, its trend of modification with the increasing of the \mathcal{N}_{coh} . The SRR R_s^0 peak values are lowered gradually with the increasing of \mathcal{N}_{coh} . As a matter of fact, the SRR peak is modified into a broad shoulder as \mathcal{N}_{coh} increases. This suppression has been analyzed, in section III B, for the $\mathcal{N}_{\text{coh}} = 2$ case at the MI resonance energies in a $W = 98$ AGNR, with excellent matching of the analytical results to the numerical results. From the spin-flipped transmission expressions, in Eqs. (47) and (48), we see that the suppression occurs for all L_{21} . Even if one of the MI, say MI-1, would have, for a particular L_{21} , a spin-flipped transmission which magnitude is greater than the individual MI's spin-flipped

transmission, $t_{n_0 n_0}^{f(0)}(b, a; 1)$, the spin-flipped transmission of the MI-2 would be lowered so that the total spin-flipped rate in the transmission is lowered. This suggests to us a physical picture for the SRR suppression in the resonance region, namely, the MIs compete among themselves for their own resonance, when they have similar resonance energies. To check on this physical picture explicitly (not shown), we shift one MI's resonance energy by changing the MI's physical parameters, such as ε_h , J , and T , and we arrive at a reduced suppression.

A further discussion on our incoherent \mathcal{N}_{coh} -MI clusters treatment for the SRR calculation is in order here. We refer to Fig. 1, our highlighted key figure, for a specific discussion example. Here our focus is on the incoherent three-MI clusters curve. Full averages have been done for both spin configurations and transverse-locations (M_1, M_2 , and M_3). The longitudinal-location average of the three MIs have been done by the $\Delta\mu$ -averaging scheme, with the SRR $1/\tau_s$ averaged over a $\Delta\mu = 0.00125$, while choosing $L_{21} = 5000$ and $L_{32} = 6000$. The incoherent three-MI clusters curve describes the situation when the phase-coherence length L_ϕ sets in to render the four-MI cluster not relevant. In other words, the round trip between the first and the fourth MIs will have to be greater than L_ϕ [66]. So, $L_\phi < 2\mathcal{N}_{\text{coh}}\Delta N_\eta$ in the units of $\sqrt{3}a$. For the case of Fig. 1, the incoherent three-MI clusters calculation is appropriate when $L_\phi < 63 \mu\text{m}$. We do not have enough information on the value of L_ϕ [66], or its temperature dependence. Yet it suffices to say that $\mathcal{N}_{\text{coh}} \leq 3$ is quite good for the given η_M . In any case, the $1/\tau_s$ characteristics in the nonresonance region remain intact, while the $1/\tau_s$ profile in the resonance region is basically known, from our study, albeit leaving the peak values as a detail subjecting to the values of L_ϕ .

IV. CONCLUSION

In conclusion, we have demonstrated two SRR suppression phenomena in long AGNRs at finite temperatures. One suppression is in the nonresonance region and the other is in the resonance region. Physical pictures behind these two SRR suppressions are different and have been revealed in our analytical analysis. We have formulated a microscopic approach for the calculation of the SRR in ballistic nanostructures. A low concentration of magnetic impurities provides the spin-flipping source.

In the nonresonance region, large SRR suppression occurs at a subband band edge. The suppression factor F_{sp} , a ratio between the $1/\tau_s$ in 2D and in AGNRs at a finite temperature, is large ($F_{\text{sp}} = 9.3, 9.7$) at 4 K, and is good ($F_{\text{sp}} = 3.2, 3.7$) even at 77 K. This is for the $W = 20$ case. For smaller W , the suppression factor is even higher.

The singular density of states at a subband band edge provides the impetus for multiple scatterings, which in turn suppress the total scattering wave function at the sites of the MIs, and lead to the suppression in the spin-flipping processes and to the formation of a dip structure in $1/\tau_s$. Our analysis shows that this singular feature is brought forth via the Green's function $G_{II}(\mu)$. Equally important, for the large SRR suppression to remain intact in finite temperatures, the profile of the SRR dip structure also matters. That is, the $1/\tau_s$ dip structure should have a gradual overall dip profile,

covering a finite μ region in the vicinity of the subband band edge. This is shown to be the case because of the contribution to $G_{\mathcal{I}\mathcal{I}}(\mu)$ from all the nonpropagating subbands, and that these contributions diminish in a gradual manner, when $|\mu|$ decreases from the subband band edge.

We have shown that the $1/\tau_s$ behavior in the nonresonance region is robust. It remains intact regardless of the number N_{coh} of MIs being involved in the coherent multiple scattering. This is shown related to the Green's function ratio $|G_{21}(\mu)/G_{11}(\mu)|$ that, when it is sufficiently small, can cause the communication between MIs via the electrons to become unimportant. The physical origin of a small $|G_{21}(\mu)/G_{11}(\mu)|$ is related to the contribution of the nonpropagating subbands to both $G_{21}(\mu)$ and $G_{11}(\mu)$. It is when, for a given μ in the central region, the contributions to $G_{21}(\mu)$ from the nonpropagating subbands becomes negligible for a large enough L_{21} , but the contribution to $G_{11}(\mu)$ from the nonpropagating subbands is important.

In the resonance region, we have found the suppression of $1/\tau_s$ at the MI resonance energies. Our analysis of the two-MI cluster case shows explicitly that the suppression occurs for all L_{21} less than the phase-coherence length L_ϕ . And that even if one of the MI would have a spin-flipped transmission greater in magnitude than that of an independent MI, the spin-flipped transmission of the other MI would be lowered so that the total spin-flipped rate in the transmission is lowered. This suggests to us a physical picture of a competition among the MIs for their own resonances, when they have similar resonance energies.

Our demonstration of the large suppression of the spin-relaxation rate from magnetic impurities, the most effective extrinsic spin-flipping source, by tuning μ to a subband band edge of the AGNRs opens up similar possibilities in other nanostructures. Nanostructures such as carbon nanotubes [67], AGNR superlattices [68–70], bilayer graphene nanoribbons [71], and nanoribbons formed from 2D materials [4] are expected to be of close relevance to the finding of this work.

ACKNOWLEDGMENTS

This work was supported by Taiwan MOST 108-2112-M-009-003 and MOST 109-2112-M-009-009 grants.

APPENDIX A: SPIN-RELAXATION RATE AND TRANSPORT COEFFICIENTS

In this Appendix, the relation between the transition rate, or the spin-relaxation rate, and the transport coefficients is established via their respective relations with the \hat{T} matrix.

The transition rate $\frac{d}{dt}|\langle\kappa_f|\kappa_i, t_0; t\rangle_s|^2$, with the effects of a potential \hat{V} fully incorporated, up to all orders, is expressed in terms of the \hat{T} matrix, given by

$$\frac{d}{dt}|\langle\kappa_f|\kappa_i, t_0; t\rangle_s|^2 = \frac{2\pi}{\hbar} \delta(E_i - E_f) |\langle\kappa_f|\hat{T}|\kappa_i\rangle|^2. \quad (\text{A1})$$

Equation (A1) was obtained in quantum mechanics textbooks [72,73] from taking an *Ansatz* approach. We show, in the following, that a direct approach for Eq. (A1) using only the time-dependent perturbation theory

presents a more lucid presentation of the physical details involved.

Consider the Hamiltonian $H = H_0 + \hat{V}e^{\eta t}$ for an infinitesimal positive η . At a sufficiently remote time t_0 in the past, where $e^{\eta t_0} \ll 1$, the initial state in the interaction picture is given by $|\kappa_i, t_0; t_0\rangle_1 = |\kappa_i\rangle$. The amplitude of the transition to the state $|\kappa_f\rangle$ at a later time t is given by $\langle\kappa_f|\kappa_i, t_0; t\rangle_s = \langle\kappa_f|e^{-iH_0 t/\hbar}\hat{U}_1(t, t_0)|\kappa_i\rangle$. Here the subscript S denotes the Schrödinger picture, $\hat{U}_1(t, t_0)$ denotes the time-evolution operator in the interaction picture, and $|\kappa_f\rangle \neq |\kappa_i\rangle$ is considered. The n th order term of the transition amplitude is given by the form

$$\langle\kappa_f|e^{-\frac{i}{\hbar}H_0 t}\hat{U}_1^{(n)}(t, t_0)|\kappa_i\rangle = \frac{e^{-\frac{i}{\hbar}E_i t + \eta n t}}{E_i - E_f + in\hbar\eta} \times \langle\kappa_f|\hat{V}(\hat{G}_{E_i}\hat{V})^{n-1}|\kappa_i\rangle, \quad (\text{A2})$$

where E_α is the energy of $|\kappa_\alpha\rangle$ and the Green's functions involved have the form $\hat{G}_{E_i} = (E_i - H_0 + in'\hbar\eta)^{-1}$, for $1 \leq n' < n$. These Green's functions are all assumed to be replaceable by that for $n' = 1$. This is achieved by keeping η infinitesimal. From Eq. (A2), the transition rate

$$\frac{d}{dt}|\langle\kappa_f|\kappa_i, t_0; t\rangle_s|^2 = \sum_{n, n'=1}^{\infty} \frac{\eta(n+n')e^{(n+n')\eta t} \langle\kappa_f|\hat{T}_n|\kappa_i\rangle \langle\kappa_f|\hat{T}_{n'}|\kappa_i\rangle^*}{(E_i - E_f + in\hbar\eta)(E_i - E_f - in'\hbar\eta)}, \quad (\text{A3})$$

where $\hat{T}_n = \hat{V}(\hat{G}_{E_i}\hat{V})^{n-1}$. Finally, Eq. (A1) is obtained from using the relation

$$\frac{(n+n')\eta}{(\varepsilon + in\hbar\eta)(\varepsilon - in'\hbar\eta)} = \frac{2\pi}{\hbar} \delta(\varepsilon), \quad (\text{A4})$$

and that $\hat{T} = \sum_{n=1}^{\infty} \hat{T}_n$ is identified as the \hat{T} -matrix that appears in the scattering theory. [72,73] The transition rate is evaluated at $t = 0$.

Now that, according to Eq. (A1), we can obtain the spin-relaxation rate of a specific process in a quasi-one-dimensional structure. Specifically, the process of an initial state $|\kappa_n, \nu\rangle$ making transition to a final state $|\kappa_{n'}, \bar{\nu}\rangle$. Both $|\kappa_n, \nu\rangle$ and $|\kappa_{n'}, \bar{\nu}\rangle$ now denote propagating channels in the quasi-one-dimensional structure. Here $|\kappa_\alpha, \nu\rangle$ denotes the electron eigenstates of H_0 , with α , and ν representing the subband and spin indices, respectively. And κ_α denotes the remaining quantum numbers of the eigenstate, such as the spin states of all the MIs and the longitudinal wave vector Q_α of the electron. The electron spin state $|\bar{\nu}\rangle = |-\nu\rangle$ is of opposite spin to the $|\nu\rangle$ state, and H_0 is degenerate in spin as the MIs effects are contained in \hat{V} . The spin-relaxation rate of this specific process is given by

$$\sum_{Q_{n'}} \frac{d}{dt}|\langle\kappa_{n'}, \bar{\nu}|\kappa_n, \nu, t_0; t\rangle_s|^2 = \mathcal{L} \frac{|\langle\kappa_{n'}, \bar{\nu}|\hat{T}|\kappa_n, \nu\rangle|^2}{\hbar^2 v_{gn'}}, \quad (\text{A5})$$

where $v_{gn'}$ is the group velocity and \mathcal{L} is the longitudinal length of the quasi-one-dimensional structure.

Connections of the matrix elements of the \hat{T} -matrix to the transmission or the reflection coefficients are obtained by a lattice-site projection of the scattered wave, given by $\langle\mathcal{J}, \bar{\nu}|\hat{G}\hat{V}|\Psi_{\kappa_n, \nu}\rangle$. Here $|\Psi_{\kappa_n, \nu}\rangle$ is the full scattering state for

the incident state $|\kappa_n, \nu\rangle$. We choose $|\kappa_n, \nu\rangle$ to be right-going. The lattice-site $|\mathcal{J}\rangle = |j, s\rangle$ is selected, for the case of transmission (reflection) coefficients, when $|\kappa_{n'}, \bar{\nu}\rangle$ and $|\kappa_n, \nu\rangle$ are moving in the same (opposite) direction, to have its longitudinal coordinate N_j greater (smaller) than all the longitudinal coordinates of the MIs. Site indices (j, s) of, respectively, the unit cell and the site-type (A/B type), are invoked for the structures formed out of graphene. In the following, we present the simpler case when all the MIs and the $|\mathcal{J}\rangle$ lattice-site are of the same-site type. The more general cases, not shown here, when the MIs occupy different-site types, are also found to give the same relation between the spin-relaxation rate of a specific process and the magnitude squares of the corresponding transmission or reflection coefficients.

On the one hand, from $\hat{V}|\Psi_{\kappa_n\nu}\rangle = \hat{T}|\kappa_n, \nu\rangle$, we have

$$\begin{aligned} \langle \mathcal{J}, \bar{\nu} | \hat{G} \hat{V} | \Psi_{\kappa_n\nu} \rangle &= \sum_{\mathcal{J}'} G_{\mathcal{J}\mathcal{J}'}(E) \langle \mathcal{J}', \bar{\nu} | \hat{T} | \kappa_n, \nu \rangle, \\ &= \frac{1}{2\pi} \sum_{\mathcal{J}'} \sum_{n'} \varphi_{n'}(j, j') g_{n'}^{\mathcal{J}\mathcal{J}'}(E) \\ &\quad \times \langle \mathcal{J}', \bar{\nu} | \hat{T} | \kappa_n, \nu \rangle, \end{aligned} \quad (\text{A6})$$

where E is the electron energy, and Eq. (B6) has been used for $G_{\mathcal{J}\mathcal{J}'}$. Decoupling of the longitudinal coordinates, N_j and $N_{j'}$, in $g_{n'}^{\mathcal{J}\mathcal{J}'}(E)$ when N_j is outside the scattering region (either $N_j \gg N_{j'}$ or $N_j \ll N_{j'}$ for all $N_{j'}$), and $N_{j'}$ is associated with the magnetic-impurity locations, allows us to rewrite $\langle \mathcal{J}, \bar{\nu} | \hat{G} \hat{V} | \Psi_{\kappa_n\nu} \rangle_{\text{prop}}$, the propagating-channel part of $\langle \mathcal{J}, \bar{\nu} | \hat{G} \hat{V} | \Psi_{\kappa_n\nu} \rangle$ in Eq. (A6) into the form

$$\begin{aligned} \langle \mathcal{J}, \bar{\nu} | \hat{G} \hat{V} | \Psi_{\kappa_n\nu} \rangle_{\text{prop}} &= \sum_{n'}' \left[\frac{-iN_y |E|}{2\beta_{n'} \sin Q_{n'}} \right] \langle \mathcal{J}, \bar{\nu} | \kappa_{n'}^{\pm}, \bar{\nu} \rangle \\ &\quad \times \langle \kappa_{n'}^{\pm}, \bar{\nu} | \hat{T} | \kappa_n, \nu \rangle. \end{aligned} \quad (\text{A7})$$

Here $|\kappa_{n'}^{\pm}, \bar{\nu}\rangle$ denotes the right(left)-going state when $|\mathcal{J}\rangle$ is located in the transmission (reflection) regime outside the scattering region, and the *primed* summation has restricted the n' th channel to the propagating ones. Equation (A7) is obtained from using the expressions of $g_{n'}^{\mathcal{J}\mathcal{J}'}(E)$ and of the subband wave function $\langle \mathcal{J}, \bar{\nu} | \kappa_{n'}^{\pm}, \bar{\nu} \rangle$ in, respectively, Eqs. (B7) and (B5).

An alternate view on Eq. (A7) provides us the following form:

$$\begin{aligned} \langle \mathcal{J}, \bar{\nu} | \hat{G} \hat{V} | \Psi_{\kappa_n\nu} \rangle_{\text{prop}} &= \sum_{n'}' t_{n'n}^f(\kappa_{n'}, \bar{\nu}; \kappa_n, \nu) \\ &\quad \times \langle \mathcal{J}, \bar{\nu} | \kappa_{n'}, \bar{\nu} \rangle, \end{aligned} \quad (\text{A8})$$

where $t_{n'n}^f(\kappa_{n'}, \bar{\nu}; \kappa_n, \nu)$ is the spin-flipped transmission coefficient. However, when \mathcal{J} is changed from located within the transmission region to within the reflection region, $t_{n'n}^f(\kappa_{n'}, \bar{\nu}; \kappa_n, \nu)$ in Eq. (A8) will be replaced by the spin-flipped reflection coefficient $r_{n'n}^f(\kappa_{n'}, \bar{\nu}; \kappa_n, \nu)$.

For a more compact presentation hereafter, the spin-flipped transmission coefficient above will be relabeled as $t_{n'n}^f(S', S)$. Here S' and S represent, respectively, the final and the initial system-spin configurations, into which spin states of all the MIs and the scattering electron have been included. Same relabeling applies also to the spin-flipped reflection coefficient.

These spin-flipped coefficients are restricted to S and S' of which the electron spin has been flipped.

From Eqs. (A8) and (A7), we obtain

$$t_{n'n}^f(S', S) = \frac{-iN_y \sqrt{3}a}{\hbar v_{gn'}(E)} \langle \kappa_{n'}, \bar{\nu} | \hat{T} | \kappa_n, \nu \rangle, \quad (\text{A9})$$

where the group velocity for the n th propagating channel [see the paragraph after Eq. (B4)] is given by

$$v_{gn}(E) = 2\sqrt{3}a\beta_n(1 + \Delta h_n) \sin Q_n / (\hbar |E|). \quad (\text{A10})$$

The expression for $r_{n'n}^f(S', S)$ is the same as in Eq. (A8) except that $\kappa_{n'}$ is replaced by $\kappa_{n'}^-$. Finally, the spin-relaxation rate, according to Eq. (A5) but now denoted by $R_s(n', S'; n, S)$ for the specific processes from (n, S, E) to (n', S', E) , wherein contributions from both transmission and reflection have been included, is given by

$$R_s(n', S'; n, S) = \frac{v_{gn'}}{N_y \sqrt{3}a} \left[|t_{n'n}^f(S', S)|^2 + |r_{n'n}^f(S', S)|^2 \right]. \quad (\text{A11})$$

Here $\mathcal{L} = N_y \sqrt{3}a$ has been used, and N_y is an even integer for AGNRs.

It is important to identify that the spin-relaxation rate $R_s(n', S'; n, S)$, given by Eq. (A11), is exactly that of the outgoing spin-flipped current for the corresponding processes. The prefactor $v_{gn'}/(N_y \sqrt{3}a)$ in Eq. (A11) is the probability current due to the subband state $|\kappa_{n'}^{\pm}, \bar{\nu}\rangle$, or simply the $|\psi_{\kappa_{n'}^{\pm}}\rangle$ state if we focus on the electron. This nice connection of the spin-relaxation rate to the outgoing spin-flipped current reassures us about our result in Eq. (A11). Most importantly, Eq. (A11) has allowed us to calculate the spin-relaxation rate by a quantum transport approach.

The thermal average of $R_s(n', S'; n, S)$, averaging over all possible incoming particle fluxes from all possible propagating n th channels, is given by the form

$$R_s^T(n', S'; S) = \frac{\sum_n' \sum_{Q_n} R_s(n', S'; n, S) [f_L(E) - f_R(E)]}{\sum_n' \sum_{Q_n} [f_L(E) - f_R(E)]}, \quad (\text{A12})$$

where $f_\alpha(E) = f_{\text{FD}}(E - \mu_\alpha)$ is the Fermi-Dirac distribution function, the primed summation is over the propagating channels for the energy E , and Q_n is the wave vector in the n th channel. The left and right electrodes of the quasi-one-dimensional system are at chemical potentials μ_L and μ_R , respectively, while they are in thermal equilibrium at the same temperature T . A quasisteady state is maintained, with $\mu_L = \mu + \Delta\mu$ and $\mu_R = \mu$. The interchangeability in Eq. (A12) of the n summation and the energy integral, which is converted from the Q_n summation, is guaranteed when $R_s(n', S'; n, S)$ has restricted the n th subband to be a propagating channel for the energy E . This allows us to express, as shown in the following, $R_s^T(n', S'; S)$ in terms of its zero-temperature limit $R_s^0(n', S'; S)$.

The zero-temperature expression $R_s^0(n', S'; S)$ can be derived from Eq. (A12), given by

$$R_s^0(n', S'; S) = \frac{\sum_n' \frac{1}{v_{gn}} R_s(n', S'; n, S)}{\sum_n' \frac{1}{v_{gn}}}, \quad (\text{A13})$$

which, according to the group velocity expression in Eq. (A10), can also be rewritten in the form

$$R_s^0(n', S'; S) = \frac{\sum_n' \frac{1}{\beta_n(1+\Delta h_n) \sin Q_n} R_s(n', S'; n, S)}{\sum_n' \frac{1}{\beta_n(1+\Delta h_n) \sin Q_n}}. \quad (\text{A14})$$

The finite temperature $R_s^T(n', S'; S)$ can then be expressed in terms of $R_s^0(n', S'; S)$, given by

$$R_s^T(n', S'; S) = \frac{\int dE \left(-\frac{\partial f_{\text{FD}}}{\partial E}\right) \left(\sum_n' \frac{1}{v_{gn}}\right) R_s^0(n', S'; S)}{\int dE \left(-\frac{\partial f_{\text{FD}}}{\partial E}\right) \left(\sum_n' \frac{1}{v_{gn}}\right)}, \quad (\text{A15})$$

where the integrands are substituted from Eq. (A13) while identifying its dependence on μ as dependence on E .

Finally, the spin-relaxation rate τ_s^{-1} at temperature T and chemical potential μ is given by

$$\frac{1}{\tau_s} = \frac{1}{\mathcal{N}_S} \sum_S \left\langle \sum_{S'}' \sum_{n'}' R_s^T(n', S'; S) \right\rangle_{\mathcal{I}}, \quad (\text{A16})$$

where averages over all possible incident spin configurations S and over possible magnetic impurity site-location configurations \mathcal{I} have been included. The primed S' summation includes S' wherein the electron spin is flipped relative to that in S . Here \mathcal{N}_S is the total number of system spin configurations. Equation (A16) describes the case when all the MIs are involved coherently in the spin-flipped multiple scatterings of the conduction electrons.

On the other hand, when the total number of MIs, \mathcal{N}_M of them, forms $\mathcal{N}_M/\mathcal{N}_{\text{coh}}$ groups of which each group behaves as a coherent magnetic-impurity cluster that contributes coherently to the spin-flipped multiple scatterings, whereas between groups the contributions to the spin-flipped scatterings can be treated as incoherent, then the spin-relaxation rate is given by

$$\frac{1}{\tau_s} = \frac{\mathcal{N}_M}{\mathcal{N}_{\text{coh}}} \frac{1}{\mathcal{N}_S} \sum_S \left\langle \sum_{S'}' \sum_{n'}' R_s^T(n', S'; S) \right\rangle_{\mathcal{I}}. \quad (\text{A17})$$

Here \mathcal{N}_S corresponds to the total number of spin configurations that is consistent with a coherent cluster involving \mathcal{N}_{coh} MIs and a conduction electron. The average over the magnetic impurity site-location configuration would then be performed within a region typically of the effective size of the cluster.

APPENDIX B: AGNR GREEN'S FUNCTION

In this section, we first present the subband wave functions of AGNRs in the presence of edge passivation, and then present the Green's function. This Appendix also serves the purpose of introducing the physical parameters used in this work.

An analytic AGNR Green's function is crucial for the extraction of important physical insights from complicated calculations and numerical results [46,74]. We show in the following that an analytic AGNR Green's function $G_{\mathcal{J}\mathcal{J}'}(E)$ can still be obtained when we include to the AGNRs additional effects, namely, effects from edge-passivation [62–64]. This is the saturation of dangling bonds by hydrogen at the AGNR edges. The most essential edge-passivation effect is to cause the *gapless* subband of the $W = 3p + 2$ AGNRs to open up a

gap [62–64]. Edge passivation also modifies the energy gaps of gapped subbands. All these subband energy-gap creation or modification can be captured by a hopping-constant modification at the AGNR edge-bonding, the bondings at the two edges that orient parallel to the AGNRs [62,63].

Explicitly, the Hamiltonian describing the edge passivation is given by

$$H_{\text{EP}} = -\delta t \sum_{N_j}' \sum_{M_j=0, W-1} [|j, A\rangle \langle j, B| + |j, B\rangle \langle j, A|], \quad (\text{B1})$$

where δt , the bulk graphene hopping constant, is chosen the value $\delta t = 0.12$ [63], so as to closely reproduce the AGNR subband energy gaps obtained from first-principle calculations [62]. The lattice site \mathcal{J} of the carbon π -orbital $|\mathcal{J}\rangle$ has $\mathcal{J} = (j, s) = (\mathbf{R}, s)$, which depicts, respectively, the graphene unit-cell position and site-type (A/B type) index. Position $\mathbf{R}_j = M_j a \hat{x} + N_j \sqrt{3} a \hat{y}$ has the transverse coordinate $0 \leq M_j \leq W - 1$, $a = 1.23 \text{ \AA}$, and W represents the number of longitudinal carbon chain in the AGNRs. We have chosen the convention that $M_j + N_j$ are even integers. As such the primed summation in Eq. (B1) denotes imposing of this convention.

For an ideal AGNR, where the edge passivation is not included, the subband index n is given by $W/2 + 1 \leq n \leq W$ for even W . The transverse subband wave function $\varphi_n(j)$ is given by

$$\varphi_n(j) = \frac{2}{\sqrt{W+1}} \sin \left[\frac{n\pi(M_j+1)}{W+1} \right], \quad (\text{B2})$$

so that $k_{nx}a = n\pi/(W+1)$ gives the quantized transverse wave vector. Focusing on the $W = 3p + 2$ AGNRs, we have the gapless subband denoted by $n_0 = 2(W+1)/3$, and the first gapped subband denoted by $n_1 = n_0 + 1$. Our major energy region of interest in this work is wherein the n_0 subband constitutes the sole propagating channel in the AGNRs.

We calculate the subband wave function by treating the H_{EP} within a perturbation scheme [63]. This is appropriate because the average $\delta t \sim \delta t/(W+1)$ per bonding is much smaller than unity. Assuming the transverse wave function $\varphi_n(j)$ to remain intact, the perturbation effects will show up in the coefficients C^s at the A and B sites. Following Ref. [63], we define two basis kets

$$|\Phi_{\mathbf{k}_n}; s\rangle = \sum_j \frac{1}{\sqrt{N_y}} e^{ik_y N_j \sqrt{3} a} \varphi_n(j) |j, s\rangle. \quad (\text{B3})$$

Matrix elements of $H_0 + H_{\text{EP}}$ with respect to these basis kets are $\langle \Phi_{\mathbf{k}_n}; s | (H_0 + H_{\text{EP}}) | \Phi_{\mathbf{k}_n}; s' \rangle$, which equals $-\tilde{h}(\mathbf{k}_n)$ when s (s') are A (B) sites, respectively, and equal zero when $s = s'$. Here, H_0 describes the ideal AGNR, and

$$\tilde{h}(\mathbf{k}_n) = h(\mathbf{k}_n) + \Delta h_n, \quad (\text{B4})$$

where $h(\mathbf{k}_n) = 1 + 2\cos(k_{nx}a) e^{ik_y \sqrt{3} a}$, and $\Delta h_n = (4\delta t/(W+1)) \sin^2(n\pi/(W+1))$. The dispersion relation for the n th subband is $E(\mathbf{k}_n, \gamma) = \gamma |\tilde{h}(\mathbf{k}_n)|$.

The subband state wave function $\langle \mathcal{J} | \psi_{\mathbf{k}_n^\pm} \rangle$, right (left)-going in its propagation, is given by

$$\langle \mathcal{J} | \psi_{\mathbf{k}_n^\pm} \rangle = \frac{e^{\pm i\gamma Q_n N_j}}{\sqrt{N_y}} \varphi_n(j) \begin{pmatrix} C^A(\mathbf{k}_n^\pm) \\ C^B(\mathbf{k}_n^\pm) \end{pmatrix}, \quad (\text{B5})$$

where $\mathbf{k}_n^\pm = (k_{nx}, \pm\gamma Q_n/(\sqrt{3}a))$, with Q_n chosen to be positive. The notation Q_n has replaced k_y when the electron energy E is our primary physical quantity of interest. Also, $C^A(\mathbf{k}_n^\pm) = 1/\sqrt{2}$, $C^B(\mathbf{k}_n^\pm) = \bar{\gamma} \tilde{h}^*(\mathbf{k}_n^\pm)/(\sqrt{2}|E|)$, $\bar{\gamma} = -\gamma$, and N_y is the total unit cells along \hat{y} in the system (N_y is even for an AGNR). All dependencies on E are kept implicit. We also define $\beta_n = -\cos(k_{nx}a)$, which is positive, to simplify our expressions below.

The tight-binding model AGNR Green's function $G_{\mathcal{J}\mathcal{J}'}(E)$, in a subband summation form, is given by [46,74]

$$G_{\mathcal{J}\mathcal{J}'}(E) = \frac{1}{2\pi} \sum_n \varphi_n(j)\varphi_n(j') g_n^{\mathcal{J}\mathcal{J}'}(E). \quad (\text{B6})$$

The same-site type reduced Green's function $g_n^{\mathcal{J}\mathcal{J}'}(E)$ for an energy E that falls within the subband, that is $\varepsilon_{n,\min} < |E| < \varepsilon_{n,\max}$, is given by

$$g_n^{\mathcal{J}\mathcal{J}'}(E) = -i \frac{\pi |E|}{2\beta_n(1 + \Delta h_n)} \frac{e^{i\gamma Q_n |L_{jj'}|}}{\sin Q_n}. \quad (\text{B7})$$

Here \mathcal{J} and \mathcal{J}' are either of the AA-type or BB-type, and $L_{jj'} = N_j - N_{j'}$. The n th subband band edges are $\varepsilon_{n,\min} = |1 + \Delta h_n - 2\beta_n|$ and $\varepsilon_{n,\max} = 1 + \Delta h_n + 2\beta_n$. In particular, $\varepsilon_{n_0,\min} = \Delta h_{n_0}$.

In our energy region of interest $\varepsilon_{n_0,\min} \leq |E| \leq \varepsilon_{n_1,\min}$, we have $Q_{n_0} \ll 1$, such that for $|E| = f\Delta h_{n_0}$ ($f > 1$), we have

$$g_{n_0}^{\mathcal{J}\mathcal{J}'}(E) \approx -i \frac{\pi}{\sqrt{1 + \Delta h_{n_0}}} \frac{e^{i\gamma Q_{n_0} |L_{jj'}|}}{\sqrt{1 - 1/f^2}}, \quad (\text{B8})$$

which clearly shows that

$$g_{n_0}^{\mathcal{J}\mathcal{J}'}(E) \approx -i\pi \frac{e^{i\gamma Q_{n_0} |L_{jj'}|}}{\sqrt{1 + \Delta h_{n_0}}}, \quad (\text{B9})$$

is quite a good approximation for Eq. (B8), even when $|E|$ is close to the subband band edge, with $f \gtrsim 2$. We note that Eq. (B9) will be used for the discussion of the SRR resonance.

When the energy E falls outside the subband energy range, the same-site type reduced Green's function $g_n^{\mathcal{J}\mathcal{J}'}(E)$ exhibits exponential decay behavior in its longitudinal-location dependence. Specifically, in the lower energy-gap region of a gapped subband, namely, $0 < |E| < \varepsilon_{n,\min}$, we have

$$g_n^{\mathcal{J}\mathcal{J}'}(E) = -\frac{\pi E}{2\beta_n(1 + \Delta h_n)} \frac{e^{-Q_n |L_{jj'}|}}{\sinh Q_n}. \quad (\text{B10})$$

In the low-energy ($|E| \ll \varepsilon_{n,\min}$) regime, we have $E^2 = (1 + \Delta h_n)^2 + 4\beta_n^2 - 4\beta_n(1 + \Delta h_n)\cosh Q_n \approx 0$, such that

$$g_n^{\mathcal{J}\mathcal{J}'}(E) \approx -\frac{2\pi E}{|4\beta_n^2 - (1 + \Delta h_n)^2|} e^{-Q_n |L_{jj'}|}. \quad (\text{B11})$$

This form in Eq. (B11) will be used for the SRR resonance discussion.

On the other hand, when $|E|$ approaches $\varepsilon_{n,\min}$ from below, that is, $|E| = \varepsilon_{n,\min} - \Delta$, we have

$$g_n^{\mathcal{J}\mathcal{J}'}(E) \approx -\frac{\pi}{2} \text{sgn}(E) \sqrt{\frac{\varepsilon_{n,\min}}{\Delta \cdot \beta_n(1 + \Delta h_n)}} \times e^{-\sqrt{\frac{\Delta \varepsilon_{n,\min}}{\beta_n(1 + \Delta h_n)}} |L_{jj'}|}. \quad (\text{B12})$$

Equation (B12) will be used for the SRR suppression discussion near subband band edges. The condition $\Delta \ll \varepsilon_{n,\min}$ has been assumed to obtain Eq. (B12). The function $\text{sgn}(x)$ returns the sign of x . It is clear from Eq. (B12) that the magnitude of $G_{\mathcal{J}\mathcal{J}'}(E)$ increases as Δ is decreasing, this is due to the dominating contribution from the n th subband to $G_{\mathcal{J}\mathcal{J}'}(E)$.

The different-site type reduced Green's function $g_{n,\text{BA}}^{\mathcal{J}\mathcal{J}'}(E)$ for an energy E that is within the subband is given by

$$g_{n,\text{BA}}^{\mathcal{J}\mathcal{J}'}(E) = -\frac{i\pi |E|}{\sqrt{2}\beta_n(1 + \Delta h_n)} \frac{e^{i\gamma Q_n |L_{jj'}|}}{\sin Q_n} \times C^B(k_{nx}, \gamma \text{sgn}(L_{jj'})Q_n), \quad (\text{B13})$$

where $|L_{jj'}| > 1$ is assumed. The AB-type reduced Green's function can be obtained from $g_{n,\text{AB}}^{\mathcal{J}\mathcal{J}'}(E) = g_{n,\text{BA}}^{\mathcal{J}\mathcal{J}'}(E)$.

Finally, the different-site type reduced Green's function, at an energy E that is outside the subband energy range, and also in the region $0 < |E| < \varepsilon_{n,\min}$, is given by

$$g_{n,\text{BA}}^{\mathcal{J}\mathcal{J}'}(E) = \frac{\pi}{2\beta_n(1 + \Delta h_n)} \frac{e^{-Q_n |L_{jj'}|}}{\sinh Q_n} \times [1 + \Delta h_n - 2\beta_n e^{-\text{sgn}(L_{jj'})Q_n}]. \quad (\text{B14})$$

- [1] N. Tombros, C. Jozsa, M. Popinciuc, H. T. Jonkman, and B. J. van Wees, Electronic spin transport and spin precession in single graphene layers at room temperature, *Nature (London)* **448**, 571 (2007).
- [2] W. Han, R. K. Kawakami, M. Gmitra, and J. Fabian, Graphene spintronics, *Nat. Nanotechnol.* **9**, 794 (2014).
- [3] S. Roche, J. Åkerman, B. Beschoten, J.-C. Charlier, M. Chshiev, S. P. Dash, B. Dlubak, J. Fabian, A. Fert, M. Guimarães, F. Guinea, I. Grigorieva, C. Schönberger, P.

Seneor, C. Stampfer, S. O. Valenzuela, X. Waintal, and B. van Wees, Graphene spintronics: the European Flagship perspective, *2D Mater.* **2**, 030202 (2015).

- [4] A. Avsar, H. Ochoa, F. Guinea, B. Özyilmaz, B. J. van Wees, and J. J. Vera-Marun, Colloquium: Spintronics in graphene and other two-dimensional materials, *Rev. Mod. Phys.* **92**, 021003 (2020).
- [5] I. Žutić, J. Fabian, and S. Das Sarma, Spintronics: Fundamental and applications, *Rev. Mod. Phys.* **76**, 323 (2004).

- [6] M. W. Wu, J. H. Jiang, and M. Q. Weng, Spin dynamics in semiconductors, *Phys. Rep.* **493**, 61 (2010).
- [7] Y. Yao, F. Ye, X.-L. Qi, S.-C. Zhang, and Z. Fang, Spin-orbit gap of graphene: First-principles calculations, *Phys. Rev. B* **75**, 041401(R) (2007).
- [8] Castro Neto, A. H. F. Guinea, N. M. R. Peres, K. S. Novoselov, and A. K. Geim, The electronic properties of graphene, *Rev. Mod. Phys.* **81**, 109 (2009).
- [9] N. M. R. Peres, Colloquium: The transport properties of graphene: An introduction, *Rev. Mod. Phys.* **82**, 2673 (2010).
- [10] D. A. Pesin and A. H. MacDonald, Spintronics and pseudospintronics in graphene and topological insulators, *Nat. Mater.* **11**, 409 (2012).
- [11] M. Shiraishi, Electrically-generated pure spin current in graphene, *Jpn. J. Appl. Phys.* **51**, 08KA01 (2012).
- [12] S. Roche and S. O. Valenzuela, Graphene spintronics: Puzzling controversies and challenges for spin manipulation, *J. Phys. D* **47**, 094011 (2014).
- [13] J. H. Garcia, M. Vila, A. W. Cummings, and S. Roche, Spin transport in graphene/transition metal dichalcogenide heterostructures, *Chem. Soc. Rev.* **47**, 3359 (2018).
- [14] W. Han and R. K. Kawakami, Spin Relaxation in Single-Layer and Bilayer Graphene, *Phys. Rev. Lett.* **107**, 047207 (2011).
- [15] R. G. Mani, J. Hankinson, C. Berger, and W. A. de Heer, Observation of resistivity detected hole spin resonance and zero-field pseudo-spin splitting in epitaxial graphene, *Nat. Commun.* **3**, 996 (2012).
- [16] B. Dlubak, M.-B. Martin, C. Deranlot, B. Sertel, S. Xavier, R. Mattana, M. Sprinkle, C. Berger, W. A. De Heer, F. Petroff, A. Anane, P. Seneor, and A. Fert, Highly efficient spin transport in epitaxial graphene on SiC, *Nat. Phys.* **8**, 557 (2012).
- [17] M. Wojtaszek, I. J. Vera-Marun, T. Maassen, and B. J. van Wees, Enhancement of spin relaxation time in hydrogenated graphene spin-valve devices, *Phys. Rev. B* **87**, 081402(R) (2013).
- [18] M. B. Lundberg, R. Yang, J. Renard, and J. A. Folk, Defect-Mediated Spin Relaxation and Dephasing in Graphene, *Phys. Rev. Lett.* **110**, 156601 (2013).
- [19] M. V. Kamalakar, A. Dankert, J. Bergsten, T. Ive, and S. P. Dash, Enhanced tunnel spin injection into graphene using chemical vapor deposited hexagonal boron nitride, *Sci. Rep.* **4**, 6146 (2014).
- [20] M. V. Kamalakar, C. Groenvelde, A. Dankert, and S. P. Dash, Long distance spin communication in chemical vapour deposited graphene, *Nat. Commun.* **6**, 6766 (2015).
- [21] M. Drögeler, C. Franzen, F. Volmer, T. Pohlmann, L. Banzarus, M. Wolter, K. Watanabe, T. Taniguchi, C. Stampfer, and B. Beschoten, Spin lifetimes exceeding 12 ns in graphene nonlocal spin valve devices, *Nano. Lett.* **16**, 3533 (2016).
- [22] B. Raes, J. E. Scheerder, M. V. Costache, F. Bonell, J. F. Sierra, J. Cuppens, J. Van de Vondel, and S. O. Valenzuela, Determination of the spin-lifetime anisotropy in graphene using oblique spin precession, *Nat. Commun.* **7**, 11444 (2016).
- [23] S. Ringer, S. Hartl, M. Rosenauer, T. Völkl, M. Kadur, F. Hopperdietzel, D. Weiss, and J. Eroms, Measuring anisotropic spin relaxation in graphene, *Phys. Rev. B* **97**, 205439 (2018).
- [24] Z. M. Gebeyehu, S. Parui, J. F. Sierra, M. Timmermans, M. J. Esplandiu, S. Brems, C. Huyghebaert, K. Garello, M. V. Costache, and S. O. Valenzuela, Spin communication over 30 μm long channels of chemical vapor deposited graphene on SiO_2 , *2D Mater.* **6**, 034003 (2019).
- [25] S. Wellenhofer, A. Stabile, D. Kochan, M. Gmitra, Y. W. Chuang, J. Zhu, and J. Fabian, Spin relaxation in fluorinated single and bilayer graphene, *Phys. Rev. B* **100**, 035421 (2019).
- [26] B. G. Márkus, P. Szirmai, K. F. Edelthammer, P. Echerlein, A. Hirsch, F. Hauke, N. M. Nemes, J. C. Chacón-Torres, B. Náfrádi, L. Forró, T. Pichler, and F. Simon, Ultralong spin lifetime in light alkali atom doped graphene, *ACS Nano* **14**, 7492 (2020).
- [27] C. Ertler, S. Konschuh, M. Gmitra, and J. Fabian, Electron spin relaxation in graphene: The role of the substrate, *Phys. Rev. B* **80**, 041405(R) (2009).
- [28] D. V. Fedorov, M. Gradhand, S. Ostanin, I. Maznichenko, A. Ernst, J. Fabian, and I. Mertig, Impact of Electron-Impurity Scattering on the Spin Relaxation Time in Graphene: A First-Principles Study, *Phys. Rev. Lett.* **110**, 156602 (2013).
- [29] D. Kochan, M. Gmitra, and J. Fabian, Spin Relaxation Mechanism in Graphene: Resonant Scattering by Magnetic Impurities, *Phys. Rev. Lett.* **112**, 116602 (2014).
- [30] J. Bundesmann, D. Kochan, F. Tkatschenko, J. Fabian, and K. Richter, Theory of spin-orbit-induced spin relaxation in functionalized graphene, *Phys. Rev. B* **92**, 081403(R) (2015).
- [31] M. R. Thomsen, M. M. Ervasti, A. Harju, and T. G. Pedersen, Spin relaxation in hydrogenated graphene, *Phys. Rev. B* **92**, 195408 (2015).
- [32] A. W. Cummings and S. Roche, Effects of Dephasing on Spin Lifetime in Ballistic Spin-Orbit Materials, *Phys. Rev. Lett.* **116**, 086602 (2016).
- [33] D. V. Tuan and S. Roche, Spin Manipulation in Graphene by Chemically Induced Pseudospin Polarization, *Phys. Rev. Lett.* **116**, 106601 (2016).
- [34] D. V. Tuan, J. M. Marmolejo-Tejada, X. Waintal, B. K. Nikolić, S. O. Valenzuela, and S. Roche, Spin Hall Effect and Origins of Nonlocal Resistance in Adatom-Decorated Graphene, *Phys. Rev. Lett.* **117**, 176602 (2016).
- [35] D. Kochan, S. Irmer, and J. Fabian, Model spin-orbit coupling Hamiltonians for graphene systems, *Phys. Rev. B* **95**, 165415 (2017).
- [36] A. W. Cummings, J. H. Garcia, J. Fabian, and S. Roche, Giant Spin Lifetime Anisotropy in Graphene Induced by Proximity Effects, *Phys. Rev. Lett.* **119**, 206601 (2017).
- [37] K. Zollner, M. Gmitra, and J. Fabian, Heterostructures of graphene and hBN: electronic, spin-orbit, and spin relaxation properties from first principles, *Phys. Rev. B* **99**, 125151 (2019).
- [38] V. G. Miranda, E. R. Mucciolo, and C. H. Lewenkopf, Spin relaxation in disordered graphene: interplay between puddles and defect-induced magnetism, *J. Phys. Chem. Solids* **128**, 169 (2019).
- [39] W. Han, K. Pi, K. M. McCreary, Y. Li, J. J. I. Wong, A. G. Swartz, and R. K. Kawakami, Tunneling Spin Injection into Single Layer Graphene, *Phys. Rev. Lett.* **105**, 167202 (2010).
- [40] H. Idzuchi, A. Fert, and Y. Otani, Revisiting the measurement of the spin relaxation time in graphene-based devices, *Phys. Rev. B* **91**, 241407(R) (2015).
- [41] W. Amamou, Z. Lin, J. van Baren, S. Turkyilmaz, J. Shi, and R. K. Kawakami, Contact induced spin relaxation in graphene

- spin valves with Al₂O₃ and MgO tunnel barriers, *APL Mater.* **4**, 032503 (2016).
- [42] D. Kochan, S. Irmer, M. Gmitra, and J. Fabian, Resonant Scattering by Magnetic Impurities as a Model for Spin Relaxation in Bilayer Graphene, *Phys. Rev. Lett.* **115**, 196601 (2015).
- [43] C. S. Chu and R. S. Sorbello, Effect of impurities on the quantized conductance of narrow channels, *Phys. Rev. B* **40**, 5941 (1989).
- [44] J. Faist, P. Guéret, and H. Rothuizen, Possible observation of impurity effects on conductance quantization, *Phys. Rev. B* **42**, 3217(R) (1990).
- [45] P. F. Bagwell, Evanescent modes and scattering in quasi-one-dimensional wires, *Phys. Rev. B* **41**, 10354 (1990).
- [46] V. M. Nguyen and C. S. Chu, Large RKKY coupling from multiple scattering in armchair graphene nanoribbons, *Phys. Rev. B* **101**, 195419 (2020).
- [47] M. A. Ruderman and C. Kittel, Indirect exchange coupling of nuclear magnetic moments by conduction electrons, *Phys. Rev.* **96**, 99 (1954).
- [48] T. Kasuya, A theory of metallic ferro- and antiferromagnetism on Zener's model, *Prog. Theor. Phys.* **16**, 45 (1956).
- [49] K. Yosida, Magnetic properties of Cu-Mn alloys, *Phys. Rev.* **106**, 893 (1957).
- [50] J. Klinovaja and D. Loss, RKKY interaction in carbon nanotubes and graphene nanoribbons, *Phys. Rev. B* **87**, 045422 (2013).
- [51] N. Klier, S. Shallcross, and O. Pankratov, Asymptotic discontinuities in the RKKY interaction in the graphene Bernal bilayer, *Phys. Rev. B* **90**, 245118 (2014).
- [52] H. González-Herrero, J. M. Gómez-Rodríguez, P. Mallet, M. Moaied, J. J. Palacios, C. Salgado, M. M. Ugeda, J.-Y. Veuillen, F. Yndurain, and I. Brihuega, Atomic-scale control of graphene magnetism by using hydrogen atoms, *Science* **352**, 437 (2016).
- [53] D. Kochan, M. Barth, A. Costa, K. Richter, and J. Fabian, Spin Relaxation in s-Wave Superconductors in the Presence of Resonant Spin-Flip Scatterers, *Phys. Rev. Lett.* **125**, 087001 (2020).
- [54] J. Fabian and S. Das Sarma, Spin Relaxation of Conduction Electrons in Polyvalent Metals: Theory and a Realistic Calculation, *Phys. Rev. Lett.* **81**, 5624 (1998).
- [55] J. Fabian and S. Das Sarma, Band-structure effects in the spin relaxation of conduction electrons, *J. Appl. Phys.* **85**, 5075 (1999).
- [56] R. J. Elliott, Theory of the effect of spin-orbit coupling on magnetic resonance in some semiconductors, *Phys. Rev.* **96**, 266 (1954).
- [57] A. Baral, S. Vollmar, S. Kaltenborn, and H. S. Schneider, Re-examination of the Elliott-Yafet spin relaxation mechanism, *New J. Phys.* **18**, 023012 (2016).
- [58] J. D. Watt, L. O'Brian, J. S. Jeong, K. A. Mkhoyan, P. A. Crowell, and C. Leighton, Magnetic impurities as the origin of the variability in spin relaxation rates in Cu-based spin transport devices, *Phys. Rev. Materials* **3**, 124409 (2019).
- [59] J. Wilhelm, M. Walz, and F. Evers, Ab initio spin-flip conductance of hydrogenated graphene nanoribbons: spin-orbit interaction and scattering with local impurity spins, *Phys. Rev. B* **92**, 014405 (2015).
- [60] Z. Chaghazardi, S. B. Touski, M. Pourfath, and R. Faez, Spin relaxation in graphene nanoribbons in the presence of substrate surface roughness, *J. Appl. Phys.* **120**, 053904 (2016).
- [61] W. Y. Rojas, C. E. P. Vilegas, and A. R. Rocha, Ab initio modelling of spin relaxation lengths in disordered graphene nanoribbons, *Phys. Chem. Chem. Phys.* **21**, 2607 (2019).
- [62] Y. W. Son, M. L. Cohen, and S. G. Louie, Energy Gaps in Graphene Nanoribbons, *Phys. Rev. Lett.* **97**, 216803 (2006).
- [63] H. Zheng, Z. F. Wang, T. Luo, Q. W. Shi, and J. Chen, Analytical study of electronic structure in armchair graphene nanoribbons, *Phys. Rev. B* **75**, 165414 (2007).
- [64] D. Gunlycke and C. T. White, Tight-binding energy dispersions of armchair-edge graphene nanostrips, *Phys. Rev. B* **77**, 115116 (2008).
- [65] C. W. J. Beenakker and H. van Houten, Quantum transport in semiconductor nanostructures, *Solid State Phys.* **44**, 1 (1991).
- [66] P. Rickhaus, R. Maurand, M. H. Liu, M. Weiss, K. Richter, and C. Schönenberger, Ballistic interferences in suspended graphene, *Nat. Commun.* **4**, 2342 (2013).
- [67] J. C. Charlier, X. Blase, and S. Roche, Electronic and transport properties of nanotubes, *Rev. Mod. Phys.* **79**, 677 (2007).
- [68] D. Rizzo, G. Veber, T. Cao, C. Bronner, T. Chen, F. Zhao, H. Rodriguez, S. G. Louie, M. Crommie, and F. R. Fischer, Topological band engineering of graphene nanoribbons, *Nature (London)* **560**, 204 (2018).
- [69] O. Groning, S. Wang, X. Yao, C. A. Pegnedoli, G. Barin, C. Daniels, A. Cupo, V. Meunier, X. Feng, A. Narita, K. Mullen, P. Ruffieux, and R. Fasel, Engineering of robust topological quantum phases in graphene nanoribbons, *Nature (London)* **560**, 209 (2018).
- [70] J. Lawrence, P. Brandimarte, A. Berdonces-Layunta, M. S. G. Mohammed, A. Grewal, C. C. Leon, D. Sanchez-Portal, and D. G. de Oteyza, Probing the magnetism of topological end states in 5-armchair graphene nanoribbons, *ACS Nano* **14**, 4499 (2020).
- [71] M. H. Oliveira, J. M. J. Lopes, T. Schumann, L. A. Galves, M. Ramsteiner, K. Berlin, A. Trampert, and H. Riechert, Synthesis of quasi-free-standing bilayer graphene nanoribbons on SiC surfaces, *Nat. Commun.* **6**, 7632 (2015).
- [72] E. Merzbacher, *Quantum Mechanics* (John Wiley and Sons, 1998).
- [73] J. J. Sakurai and J. Napolitano, *Modern Quantum Mechanics* (Pearson, 2011).
- [74] C. H. Chiu and C. S. Chu, Nodal adsorbate bound states in armchair graphene nanoribbons: Fano resonances and adsorbate recognition in weak disorder, *Phys. Rev. B* **90**, 195436 (2014).